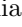








# The anti-aligned spin of GW191109: glitch mitigation and its implications

Rhiannon Udall <sup>1,2,\*</sup> Sophie Hourihane <sup>1,2,†</sup> Simona Miller <sup>1,2,‡</sup> Derek Davis <sup>1,2,§</sup> Katerina Chatziioannou <sup>1,2,¶</sup> Max Isi <sup>3,\*\*</sup> and Howard Deshong <sup>4,2,††</sup>

<sup>1</sup>*Department of Physics, California Institute of Technology, Pasadena, California 91125, USA*

<sup>2</sup>*LIGO Laboratory, California Institute of Technology, Pasadena, California 91125, USA*

<sup>3</sup>*Center for Computational Astrophysics, Flatiron Institute, New York, NY 10010, USA*

<sup>4</sup>*Schmidt Academy for Software Engineering, Pasadena, California 91125, USA*

(Dated: January 20, 2025)

With a high total mass and an inferred effective spin anti-aligned with the orbital axis at the 99.9% level, GW191109 is one of the most promising candidates for a dynamical formation origin among gravitational wave events observed so far. However, the data containing GW191109 are afflicted with terrestrial noise transients, i.e., detector glitches, generated by the scattering of laser light in both LIGO detectors. We study the implications of the glitch(es) on the inferred properties and astrophysical interpretation of GW191109. Using time- and frequency-domain analysis methods, we isolate the critical data for spin inference to 35 – 40 Hz and 0.1 – 0.04 s before the merger in LIGO Livingston, directly coincident with the glitch. Using two models of glitch behavior, one tailored to slow scattered light and one more generic, we perform joint inference of the glitch and binary parameters. When the glitch is modeled as slow scattered light, the binary parameters favor anti-aligned spins, in agreement with existing interpretations. When more flexible glitch modeling based on sine-Gaussian wavelets is used instead, a bimodal aligned/anti-aligned solution emerges. The anti-aligned spin mode is correlated with a weaker inferred glitch and preferred by  $\sim 70 : 30$  compared to the aligned spin mode and a stronger inferred glitch. We conclude that if we assume that the data are only impacted by slow scattering noise, then the anti-aligned spin inference is robust. However, the data alone cannot validate this assumption and resolve the anti-aligned spin and potentially dynamical formation history of GW191109.

## I. INTRODUCTION

Reported in the third gravitational wave (GW) transient catalog (GWTC-3) [1], GW191109\_010717 (more concisely GW191109) stands out among existing binary black hole (BBH) signals. With source-frame primary and secondary masses of  $m_1 = 65^{+11}_{-11} M_\odot$  and  $m_2 = 47^{+15}_{-13} M_\odot$  (90% symmetric credible intervals), it is among the most massive events. Furthermore, there is significant support for black hole (BH) spins anti-aligned with the orbital angular momentum: the mass-weighted effective spin [2–4] is  $\chi_{\text{eff}} = -0.29^{+0.42}_{-0.31}$ . For these reasons, as well as support for unequal masses,  $q = m_2/m_1 = 0.73^{+0.21}_{-0.24}$ , spin-precession, and hints of eccentricity [5, 6], the binary is potentially of dynamical and/or hierarchical origin [7, 8] and impacts population inference [9, 10].

Multiple GW191109 properties hint toward a dynamical origin. High masses, above the pair-instability supernova (PISN) limit of 45 – 70  $M_\odot$  (depending on modeling assumptions) [11, 12], may require a hierarchical mechanism in order to form and merge. Asymmetric masses, in particular, might imply the merger of a second- and

a first-generation BH [7]. Furthermore, population synthesis simulations of isolated formation scenarios typically find little support for spins anti-aligned with the orbital angular momentum, unless supernova kicks are exceptionally high [8, 13, 14]. Finally, eccentricity would also be challenging to explain except by dynamical processes [5, 15, 16], due to the rapid orbit circularization by GW emission [17].

Given their astrophysical implications, the inferred properties of GW191109 are worth scrutinizing. The first potential source of systematics is the waveform used to model the signal. GWTC-3 employed the IMRPHENOMXPHM [18] and SEOBNRv4PHM approximants [19], with inference performed by BILBY [20, 21] and RIFT [22] respectively. Both models include the physical effects of higher-order modes and spin-precession, and headline results (as quoted above) are their average. However, GW191109 is flagged for systematic differences between approximants [1], especially for the binary inclination (edge-on versus face-on/off respectively) and the longer  $\chi_{\text{eff}} > 0$  tail with IMRPHENOMXPHM. A third waveform, NRSUR7DQ4 [23], was employed in Ref. [24]. A direct surrogate of numerical relativity simulations, NRSUR7DQ4 is expected to be the most accurate available model for systems with high masses and spins [23–25]. These results bolster the evidence for dynamical origin, with a more negative spin,  $\chi_{\text{eff}} = -0.38^{+0.21}_{-0.20}$ , asymmetric masses,  $q = 0.65^{+0.20}_{-0.19}$ , and a precessing spin parameter [26] of  $\chi_p = 0.59^{+0.26}_{-0.27}$ . While waveform systematics remain relevant, the broad agreement between three waveforms (including a direct

\* rudall@caltech.edu

† sohour@caltech.edu

‡ smiller@caltech.edu

§ dedavis@caltech.edu

¶ kchatziioannou@caltech.edu

\*\* misi@flatironinstitute.org

†† hdeshong@caltech.edu

surrogate to numerical relativity) that  $\chi_{\text{eff}} \lesssim 0$  to varying credibility, suggests that subsequent interpretations of its formation history remain valid.

A second potential source of systematics concerns modeling the detector noise. Around GW191109’s arrival, both LIGO [27] detectors experienced a terrestrial noise transient known as a scattered light glitch [1, 28, 29]. The Virgo detector [30] was offline at this time, and so only the LIGO detectors contributed to the observation. In LIGO Hanford (LHO), the glitch power was at a nadir while the event was in the detection band, making its impact on the inferred parameters negligible, see App. A. As such, we ignore the LHO glitch going forward. By contrast, glitch power in the Livingston detector (LLO) was directly coincident in time and frequency with the signal, a circumstance which could bias astrophysical inference [31–35]. Specifically, glitch power extends up to  $\sim 40$  Hz, coincident with the signal, see Fig. 1. Spin parameters might be particularly susceptible to such data quality issues due to the relatively smaller imprint they leave on signals compared to, e.g., the BH masses. For example, GW200129 shows evidence of spin-precession [1, 25], but its significance depends on how the glitch that overlapped that signal is modeled [33, 36].

The headline GWTC-3 results were obtained after an estimate for the glitch had been subtracted from the data. The two-step process involved first modeling the signal and the glitch with a flexible sum of coherent and incoherent wavelets respectively with BAYESWAVE [37–39]. Second, a fair draw from the glitch posterior was subtracted and the system parameters were inferred as quoted above. This procedure has been shown to generally lead to unbiased mass and (aligned) spin inference [31, 34]. However, uncertainties remain related to BAYESWAVE’s glitch model and in the fair draw chosen to be subtracted. These effects were investigated in Ref. [28], albeit with a simpler waveform model with single-spin precession and no higher-order modes, IMRPHENOMPv2 [40]. Glitch mitigation was found to affect the  $\chi_{\text{eff}}$  inference by a similar amount as waveform systematics. Completely removing the glitch-affected data, i.e. all LLO data below 40 Hz, instead resulted in a dramatic shift of  $\chi_{\text{eff}}$  to positive values  $\chi_{\text{eff}} = 0.27^{+0.24}_{-0.48}$ .

The stark impact of glitch-affected data on astrophysically-impactful spin inference motivates our study. In Sec. III we extend Ref. [28] to explore the manner in which the data inform the system parameters. Using NRSUR7DQ4 and a frequency-domain analysis, we find that the LLO data between 30 and 40 Hz are crucial for spin inference: excluding 30 – 40 Hz data shifts the probability of  $\chi_{\text{eff}} < 0$  from 99.4% to 32.2%, effectively wiping out any preference for anti-aligned spins. A similar time-domain analysis [41] highlights the role of the data 0.1 – 0.04 s prior to merger. These data, which inform the  $\chi_{\text{eff}} < 0$  measurement, coincide in time and frequency with excess power in LLO, see Fig. 2 and in particular the excess power at  $\sim 36$  Hz. To check whether such dramatic shifts in support for  $\chi_{\text{eff}} < 0$

are possible from Gaussian noise alone, we analyze 100 simulated signals consistent with GW191109. We find that shifts of this magnitude are unlikely but not impossible as 6% of the simulations experience a larger shift than GW191109.

In Sec. IV, we focus on the 36 Hz excess power and address the key question: is the excess power part of the signal (and hence  $\chi_{\text{eff}} < 0$ ) or is it part of the glitch (and hence inference has been affected by systematics)? Rather than the two-step process of glitch fitting and subtraction, we perform a full analysis where we *simultaneously* model both the signal and the glitch. Using a physically motivated model for scattered light glitches [29] we find  $\chi_{\text{eff}} < 0$  at the 99.9% level using NRSUR7DQ4. We attribute this to the fact that the 36 Hz power is more contained in time than expected for scattered light glitches that are characterized by extended arches in time-frequency. This analysis, therefore, attributes the 36 Hz power to the signal and thus prefers  $\chi_{\text{eff}} < 0$ . It is, however, possible that not all terrestrial power is due to scattered light or that the physical model of Ref. [29] does not capture all scattered light power. Instead, using a more flexible model for the glitch based on wavelets and BAYESWAVE and IMRPHENOMXPHM we obtain a bimodal solution for the spin. One mode, preferred at the 70 : 30 level, attributes most of the 36 Hz power to the signal and results in  $\chi_{\text{eff}} < 0$ . The second mode attributes this power to the glitch and results in  $\chi_{\text{eff}} > 0$ . Given the low signal-to-noise ratio (SNR) of the 36 Hz power, these results are impacted by the priors of the glitch model parameters at the few percent level.

In Sec. V we summarize our conclusions. Physically grounded assumptions about the behavior of scattered light glitches lend support to  $\chi_{\text{eff}} < 0$  for GW191109, and thus a dynamical origin. However, both systematic limitations on scattered light models and statistical uncertainty due to low SNR of the excess power and the impact of glitch priors prevent us from making that determination confidently. While the crucial 36 Hz power is not part of the scattered light glitch as modeled in Ref. [29], we cannot rule out glitch mismodeling or other types of terrestrial noise.

## II. MODELING SIGNALS AND GLITCHES

The relevant data contain the GW191109 signal, glitch power, and Gaussian noise. In this section, we describe how we model the signal (Sec. II A), the glitch (Sec. II B), and methods for glitch mitigation (Sec. II C). We focus on the respective strengths and weaknesses of each approach and what unique information each supplies. All analyses model the Gaussian noise component with the power spectral densities (PSDs) from the GWTC-3 data release [42, 43]. Detailed settings and identification numbers for all analyses are given in Table I in App. B.

## A. Modeling the Compact Binary Signal

We use both time- and frequency-domain techniques to model the signal with either waveform approximants for compact binary signals or, more generically, with sine-Gaussian wavelets. All analyses consider data surrounding the nominal trigger time of GW191109, GPS time 1257296855.22, and employ a sampling rate of 1024 Hz, with the maximum analysis frequency set to 7/8 of the Nyquist frequency. Unless otherwise noted, analyses that model only the compact binary (and not the glitch) use a minimum frequency of 20 Hz in both detectors. We use standard compact-binary priors [21], notably uniform in detector-frame component masses and spin magnitude and orientation.

### 1. Frequency-domain inference

Frequency domain analyses with waveform approximants are based on BILBY [20, 21] with its implementation of the DYNASTY sampler [44] and BAYESWAVE [32], both analyzing 4 s of data. The former models the signal with NRSUR7DQ4 [23] and the latter with IMRPHENOMXPHM [18] (though for consistency we also perform checks with the former using IMRPHENOMXPHM in App. C). NRSUR7DQ4 supports a minimum mass ratio of 0.25 and minimum detector-frame chirp mass of  $35 M_{\odot}$ ; neither restriction affects the analysis. We extend into the extrapolation region in spins, setting a maximum spin magnitude of 0.99. For comparison, we also perform analyses with BAYESWAVE where the signal is modeled as a flexible sum of coherent sine-Gaussian wavelets [37, 39]. Settings are similar to the glitch wavelet analysis described in Sec. II B 2, only here, the wavelets are coherently projected across the two detectors rather than being independent.

### 2. Time-domain inference

While GW inference is typically conducted in the frequency domain for computational efficiency, it can equivalently be conducted in the time domain [45–48]. Frequency domain analyses are non-local in time; to avoid non-trivial likelihood modifications [49], time-domain inference is necessary in order to isolate purely temporal features of the data. Below, we truncate the GW191109 data at different times around the 36 Hz excess power, and independently conduct inference on the pre- or post-cutoff-time data. For this, we use the time-domain inference code employed in Ref. [41] to study the GW190521 properties and which was based on time-domain implementations targeting post-merger data [46, 47]. All time-domain results are based on regions of 1 s of data around GW191109’s trigger time and employ NRSUR7DQ4 [23]. The same PSDs are used in the time domain analyses

are the same as those in the frequency domain analyses, i.e. from the GWTC-3 data release [42].

## B. Modeling the Glitch

Both LHO and LLO experienced slow scattering noise around the time of GW191109. We use two models for the glitch power: a physically motivated model tailored to slow scattering, implemented in BILBY, and a more flexible wavelet model, implemented in BAYESWAVE.

### 1. Physically-parameterized scattering

As the name implies, scattered light glitches arise due to laser light that scatters off the main beam path, bounces off a surface, and recombines with the main beam [29, 50–53]. During periods of significant ground motion when the scattering surface moves, this light acquires a phase offset, resulting in excess noise. Figure 1 shows a spectrogram of the LLO data, along with the frequency tracks of the scattering excess noise as predicted by a witness data stream that captured the motion of the suspected scattering surface. The effect of scattering is most easily discernible 3 s before the signal, taking the form of a “stack” of arches, which is characteristic of slow scattering. Slow scattering results from low-frequency ground motion,  $\sim 0.05$ – $0.3$  Hz, driving slow movement of the scattering surface [51]. This induces phase noise with frequency [50]

$$f(t) = \left| \frac{2v_{sc}(t)}{\lambda} \right|, \quad (1)$$

with  $v_{sc}(t)$  being the velocity of the scattering surface and  $\lambda = 1064$  nm is the wavelength of the laser. In order for the glitch frequency to reach the analysis band, the scattered light must bounce multiple times, yielding a fixed frequency ratio between arches as the same amount of phase offset is accumulated with each successive bounce.

This picture forms the basis for a parametrized model for slow scattering that treats the scattering surface as a simple harmonic oscillator. We use the physically parameterized scattering model proposed in Ref. [29]. The model is a sum of frequency-modulated sinusoids with  $2N + 4$  parameters, where  $N$  is the number of arches:

$$g(t) = \sum_{k=0}^N A_k \sin \left[ \frac{f_{h,0} + k\delta f_h}{f_{\text{mod}}} \sin \left( 2\pi f_{\text{mod}}(t - t_c) \right) + \phi_k \right]. \quad (2)$$

The peak frequency of the lowest arch is  $f_{h,0}$  and the spacing in peak frequencies between adjacent arches is  $\delta f_h$ , such that the peak frequency of the  $k$ th arch is  $f_{h,0} + k\delta f_h$ .<sup>1</sup> The modulation frequency  $f_{\text{mod}}$  corre-

<sup>1</sup> Unlike Ref. [29], we fix the frequency ratio between arches to  $\delta f_h$ , thus eliminating  $N - 1$  parameters.

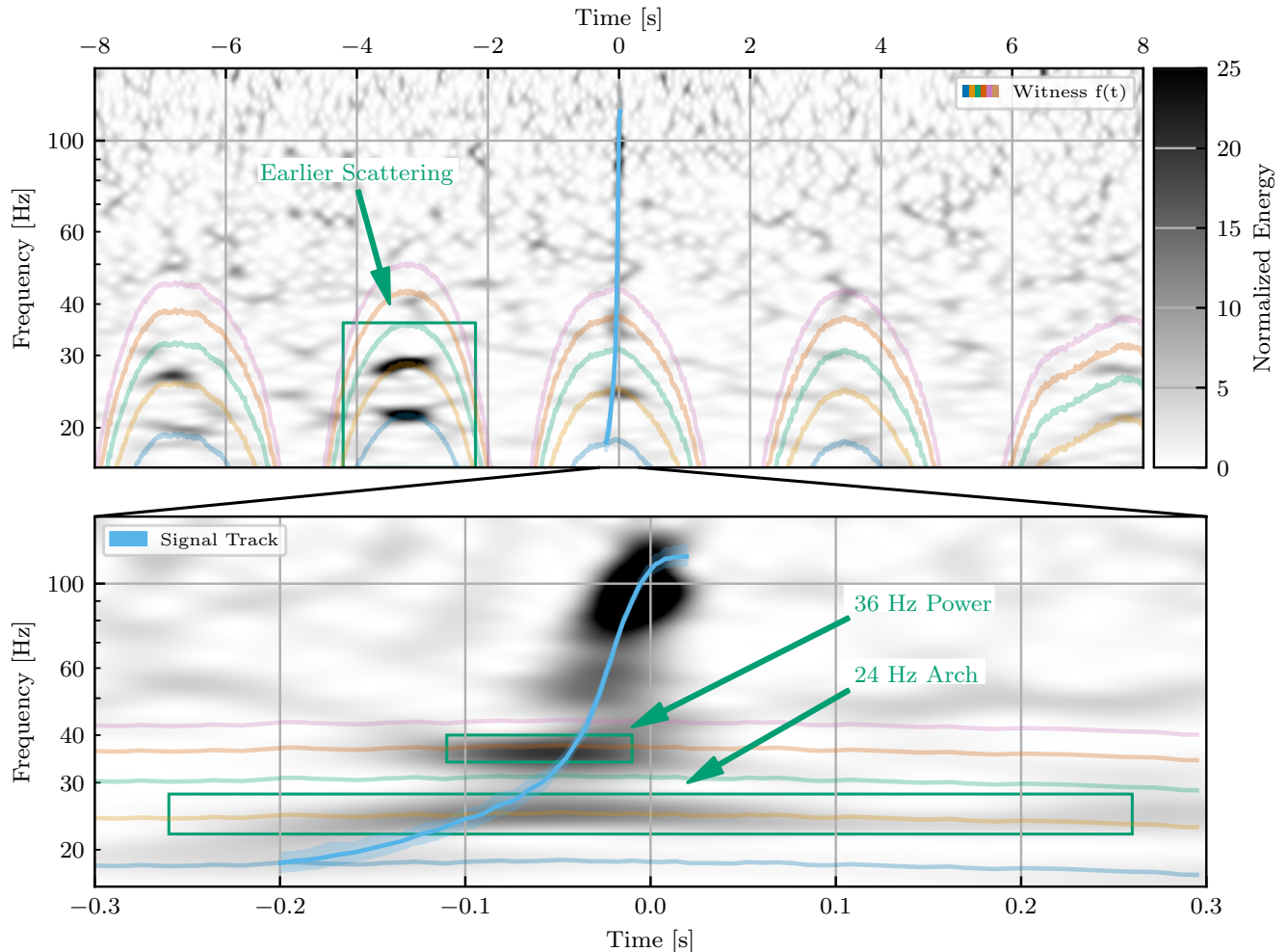


FIG. 1. Spectrograms of the original (before glitch mitigation) data in LLO centered around the time of GW191109. The top panel shows  $\pm 8$  s of data, while the bottom panel zooms in around the event. Onto this, we plot the time-frequency tracks of the scattered light glitch, as predicted by the motion observed in the witness channel L1:SUS-ETMX\_L2\_WIT\_L\_DQ. This is the witness to the penultimate stage of the reaction chain pendulum for the X-arm end test mass. The scattering surface is the final stage of the reaction chain, and so this witness does not perfectly capture the motion of the scattering surface; to compensate, we apply a static coefficient of 1.38 to the predicted frequency, such that it is calibrated to the prominent scattering arches  $\sim 3$  s before the event. We also plot the inferred signal from a NRSUR7DQ4 analysis of full-bandwidth data after glitch subtraction (Run 1 in Table I). We annotate three regions of interest: the prominent scattering before the event (top panel), the long-duration excess power at 24 Hz (bottom panel), and the short-duration excess power at 36 Hz (bottom panel). Both the 24 Hz and the 36 Hz excess power coincide with expected glitch arches, however only the former has an arch-like shape.

sponds to the motion of the scattering surface (and hence the driving ground motion) and sets the width of the arch, while  $t_c$  is the time of peak frequency. Each arch  $k$  further has an independent amplitude  $A_k$  and phase  $\phi_k$ .

Priors on these parameters reflect the physical slow scattering picture. For  $\delta f_h$  and  $f_{h,0}$ , we place uniform priors around the approximate values read from Fig. 1,  $\delta f_h \sim \mathcal{U}(5, 8)$  Hz and  $f_{h,0} \sim \mathcal{U}(18, 20)$  Hz, while for  $\phi_k$  we set a uniform periodic prior,  $\phi_k \sim \mathcal{U}(0, 2\pi)$ . We employ two sets of priors on  $f_{\text{mod}}$ . “Physical” priors limit the modulation frequency to the microseism band  $f_{\text{mod}} \sim \mathcal{U}(0.05 - 0.3)$  Hz [51]. “Targeted” priors fur-

ther restrict the modulation based on the witness motion  $f_{\text{mod}} \sim \mathcal{U}(0.05 - 0.15)$  Hz. While the former choice is more agnostic, the latter maximizes information from witness channels. Since the detector sensitivity varies by orders of magnitude in the frequency region spanned by the arches, we explore both a uniform and log-uniform amplitude for the amplitude  $A_k$ . We do not impose a relation between the arch amplitudes; while amplitudes might be expected to decrease with each arch, this is not universally the case [29].

The number of arches  $N$  is fixed and not a parameter of the model that is varied, unlike the flexible glitch model

with BAYESWAVE discussed in Sec. II B 2. The choice of the number of arches, therefore, impacts the results, especially for the uniform amplitude prior. Motivated by Fig. 1 we set  $N = 5$ , a choice which we investigate in App. D. All analyses that model the glitch with the slow scattering model further employ a reduced minimum frequency of 16 Hz in LLO. Though the signal SNR,  $\rho$ , is negligible between 16 and 20 Hz (0.16% of  $\rho^2$  in LLO), this setting accommodates the  $\sim 18$  Hz arch, which in turn informs the upper arches.

If the glitch overlapping GW191109 is consistent with the physical picture that motivates the slow scattering model, corresponding analyses provide the most sensitive results on the system properties. However, the model is also restricted to an interpretation of slow scattering and does not provide a means to test this assumption. If other non-Gaussian transient noise is present or if the physical picture does not fully capture the glitch morphology, biases might arise.

### 2. Wavelet glitch model

To mitigate against glitch modeling systematics, we also employ a more flexible approach with BAYESWAVE which models transient, non-Gaussian noise independently in each detector as sums of sine-Gaussian, Morlet-Gabor wavelets [37, 39]. Such wavelets are an overcomplete basis and any smooth function can be described with some linear combination of wavelets. Thus, this glitch model is flexible enough to fit a wide range of non-Gaussian transients without fine-tuning, including slow scattering [32, 34]. Unlike the parameterized scattering model, the BAYESWAVE glitch model is purely phenomenological, though motivated by the generic morphology of the LIGO glitches. Each wavelet is described by 5 parameters: central time  $t$  and frequency  $f$ , quality factor  $Q$  describing how quickly it is damped, amplitude  $A$ , and phase  $\phi$ . We employ uniform priors over all parameters other than the amplitude, which is set through a prior on the wavelet SNR that peaks at 5 [37]. In addition to these parameters, the number of wavelets in each detector is also a variable and sampled over with a uniform prior. Uniform prior bounds are wide enough so as to not affect the posterior.

## C. Glitch Mitigation Approaches

We employ three approaches to mitigate and study the impact of the glitch on inference: (1) discarding the affected data, (2) subtracting an estimate for the glitch from the data, and (3) simultaneously modeling the signal and glitch and obtaining source parameters for the former by marginalizing over the latter.

### 1. Discarding Affected Data

The most straightforward way to mitigate the impact of a glitch is to discard the affected data, either by band-passing in the frequency domain or by analyzing limited segments in the time domain [28, 31, 33]. While straightforward to implement, such methods forego all information in the discarded data, making them suboptimal. We instead follow Refs. [28, 33] and discard glitch-affected data only as a consistency check and to study the impact of the glitch, or its residual, on inference. Such analyses confirm that mitigation is necessary and provide insights into the detailed behavior of the data.

### 2. Subtraction of a Glitch Estimate

GWTC-3 results on GW191109 were obtained after an estimate of the glitch was subtracted from the data [1]. In most cases, the estimate for the glitch is a fair draw from a previous analysis with BAYESWAVE [1, 54–56] but estimates generated from witness channels such as in GWSUBTRACT are also possible [28]. Glitch-subtracted data are then used for downstream source inference. This method retains all the data and information available and is, therefore, more suitable for production analyses. However, its efficacy hinges on the subtracted glitch estimate since the true morphology of the glitch cannot be perfectly known. In the fair draw case, the expected glitch residual SNR is non-zero due to statistical uncertainty [57]. In the witness channel case, the relevant transfer functions induce further systematic and/or statistical uncertainty [33]. Residual glitch power that could bias inference is therefore expected.

### 3. Marginalization Over Glitch Realizations

Since selecting a single glitch estimate to subtract results in residual glitch SNR, the final method is to marginalize over the glitch. This approach is the most robust, but it is also typically more difficult to implement. Given some parameterized glitch model  $g(\phi)$ , we can model the data as:

$$d = n + h(\theta) + g(\phi) \quad (3)$$

From this, we may extend the typical likelihood in a single detector to include the glitch:

$$\ln \mathcal{L}(d|\theta, \phi) = -\frac{1}{2} \sum_k \left\{ \frac{[d_k - h_k(\theta) - \phi_k(\phi)]^2}{S_n(f_k)} + \ln(2\pi S_n(f_k)) \right\} \quad (4)$$

Where  $k$  indexes the frequency bins being summed over, and  $S_n(f_k)$  is the power spectral density in the  $k$ 'th frequency bin. In detectors without glitches this reduces to the standard CBC likelihood, and they combine in the usual way. Using this formulation, one may then sample over both  $h(\theta)$  and  $g(\phi)$  simultaneously. From these samples, one may then marginalize over  $\phi$  to produce CBC posteriors which reflect uncertainties in the modeling of the glitch.

We perform three glitch-marginalized analyses on GW191109. First, using BAYESWAVE, we combine the signal model with IMRPHENOMXPHM described in Sec. II A 1 and the sine-Gaussian glitch model described in Sec. II B 2. Compared to previous relevant analyses [32–34] we have extended the signal model to support waveforms with spin-precession and higher-order modes. Second, again using BAYESWAVE, we combine the coherent wavelet signal model described in Sec. II A 1 and the incoherent wavelet glitch model described in Sec. II B 2 [35]. This analysis uses a more flexible—and thus less sensitive—model for the GW signal; it is thus used as an additional check. Even though BAYESWAVE has the capability to also marginalize over the Gaussian noise PSD [38, 58], we fix it for consistency with other analyses and since its effect on source inference is generally minimal [59]. Third, we implemented the physically-motivated scattered light glitch model of Sec. II B 1 in BILBY. This allows us to jointly use the slow scattering model and the NRSUR7DQ4 approximant for the signal.

### III. UNDERSTANDING THE GW191109 INFERENCE

In this section, we explore the relation between the GW191109 inference, especially the  $\chi_{\text{eff}} < 0$  measurement, and the glitch-affected data. In Fig. 1 we show spectrograms of the original data (without any glitch mitigation) in LLO at the time of the event.<sup>2</sup> Arch-like traces (multiple colors) show the glitch time-frequency tracks as predicted by a witness channel. The light blue track corresponds to GW191109 as inferred with NRSUR7DQ4 from data after the glitch was subtracted (Run 1 in Table I). The upper panel presents 16 s of data; scattering arches are visible leading up to the event. In the bottom panel, we focus on the vicinity of the signal and highlight the intersection of the signal track with visible excess power along the projected scattering tracks. The first is at  $\sim 24$  Hz and has the expected duration and morphology of a scattering arch. The second is at  $\sim 36$  Hz and while it coincides with the glitch track predicted by the witness, the excess power duration is short and does not match the expected behavior of slow scattering. As noted in Ref. [28], this 36 Hz excess power

is not included in the original BAYESWAVE glitch reconstruction and thus not subtracted in the GWTC-3 data.

We begin by confirming and extending the results of Ref. [28] with NRSUR7DQ4. Analyzing data from each detector separately (Runs 8 and 9 in Table I) we confirm that the measurement is driven solely by LLO, which prefers  $\chi_{\text{eff}} < 0$  at 99.6%, compared to 20.0% in LHO. Coherent analysis of both detectors (Run 1 in Table I) tends to the LLO conclusion due to LLO's higher sensitivity in the relevant frequency range, shown below to be 20–40 Hz. Indeed, the maximum likelihood waveform from the coherent analysis accumulates 20% (8%) of its SNR squared in LLO (LHO) for frequencies below 40 Hz. This estimate further suggests that LHO data cannot aid in determining whether the critical  $\sim 36$  Hz excess power is part of the signal or the glitch.

Similar differences in parameter inference per detector are present for other parameters as well, notably the detector-frame total mass  $M$  and luminosity distance  $D_L$ ; see footnote 3 for a discussion of the correlation between  $\chi_{\text{eff}}$  and  $D_L$ . For example, in individual detector analyses (Runs 8 and 9 in Table I) the detector-frame total mass is  $M = 133^{+14}_{-14} M_{\odot}$  ( $M = 162^{+21}_{-20} M_{\odot}$ ) in LLO (LHO), while the luminosity distance is  $D_L = 1630^{+1360}_{-850}$  Mpc ( $D_L = 2760^{+2300}_{-1570}$  Mpc) in LLO (LHO). The corresponding source-frame total mass remains the same as the increases in detector-frame mass and distance effectively “cancel out”. Though different, these estimates are still consistent with each other within statistical uncertainties so there is no indication of a discrepancy across detectors as was the case for GW200129 [33]. Moreover, these differences do not lead to diverging astrophysical interpretations like the  $\chi_{\text{eff}}$  inference; we therefore focus on the latter in what follows.

#### A. Tracing inference across frequencies

To more precisely track the origin of the  $\chi_{\text{eff}} < 0$  measurement across LLO data, we perform a series of coherent 2-detector analyses where we successively restrict the LLO frequencies, incrementing the minimum frequency  $f_L$  by 5 Hz from 20 to 45 Hz (Runs 1–5 in Table I). We use the glitch-subtracted data where the 24 Hz arch from Fig. 1 has been subtracted, but the 36 Hz excess power has not [1]. A subset of these results are shown in Fig. 2 (pink shading). The top panel shows a spectrogram of the glitch-subtracted data; compared to Fig. 1, there is no excess noise at  $\sim 24$  Hz.

Marginalized posteriors for  $\chi_{\text{eff}}$  are shown in the bottom panel. The legend denotes the percentage of the total SNR squared  $\rho^2$  (computed based on the maximum-likelihood full-band signal) that remains in the analysis window after each restriction. Removing data between 20–30 Hz (solid vs dashed horizontal lines in the top panel and histograms in the bottom panel) or 30–35 Hz (dashed vs dotted) removes 6% of  $\rho^2$  but does not dramatically alter inference:  $\chi_{\text{eff}} < 0$  is still preferred at

<sup>2</sup> A similar plot for the LHO data showing that the scattered light glitch does not overlap with the signal is given in App. A.

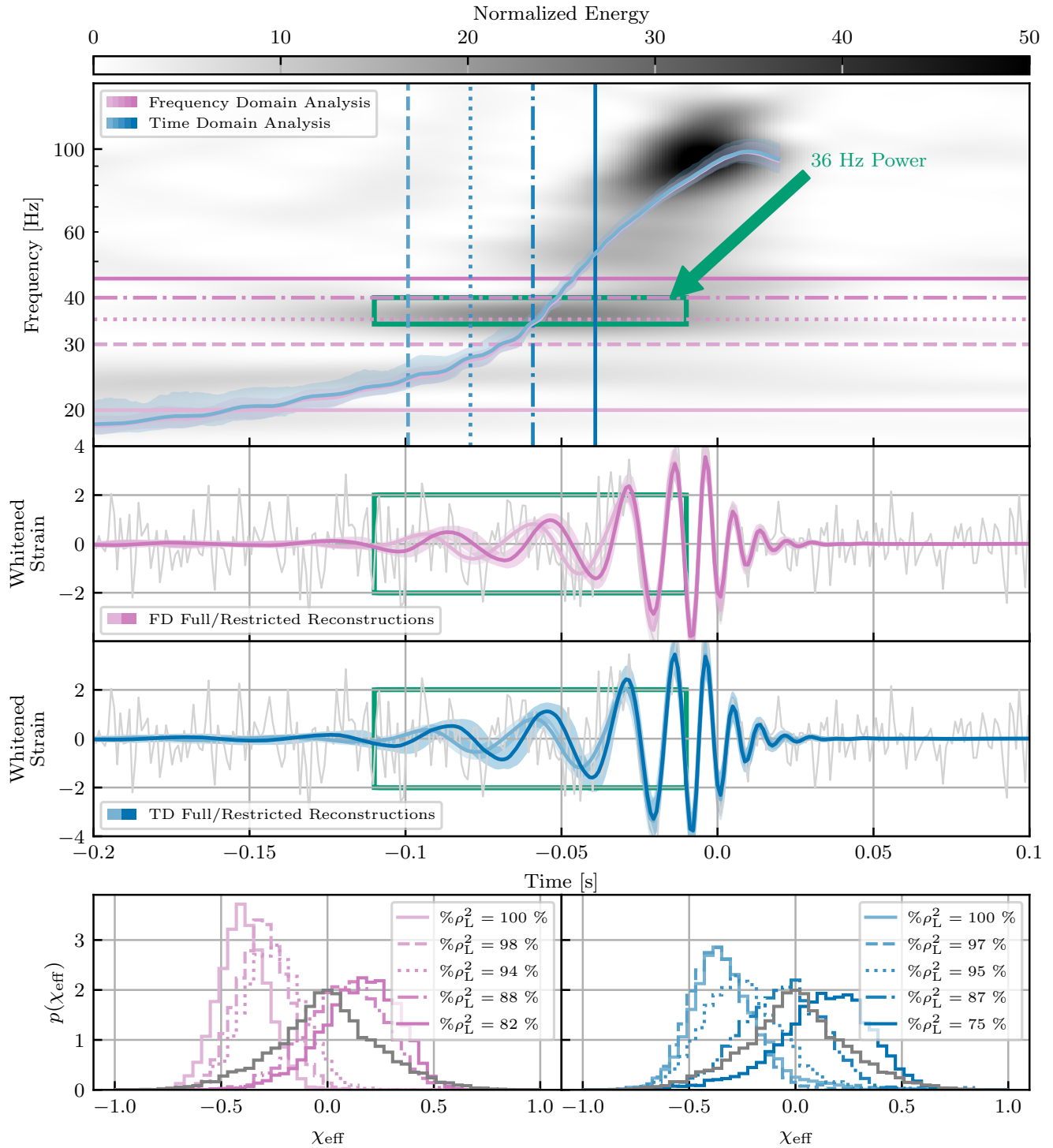


FIG. 2. Tracing the  $\chi_{\text{eff}}$  inference across frequencies and times. The top panel shows the spectrogram of the glitch-subtracted data around GW191109, with residual excess power at 36 Hz highlighted along with the signal track. We progressively remove data in the frequency domain (pink) and the time domain (blue) and reanalyze the restricted data. Vertical and horizontal lines in the top panel denote the time and frequency cuts, respectively; only data to the left or above these lines are analyzed. The two middle panels show the whited time-domain data (grey) and signal reconstruction (pink and blue). Lighter colors correspond to the analyses of the full data, while darker colors correspond to the most restricted data (frequencies above 40 Hz and times from  $-0.04$  s before merger onwards). The bottom row shows the  $\chi_{\text{eff}}$  prior (gray) and  $\chi_{\text{eff}}$  marginal posteriors from analyses with varying levels of data restriction, each corresponding to the lines on the top panel. The legend notes the SNR squared  $\rho^2$  fraction in Livingston that remains in the analysis band after each data restriction.

96.3% for  $f_L = 35$  Hz. Such small shifts are likely consistent with the SNR reduction and regression to the prior (gray). Removing data 35–40 Hz (dotted vs dot-dashed) removes an additional 6% of  $\rho^2$  and instead results in an abrupt shift in  $\chi_{\text{eff}}$ , with  $\chi_{\text{eff}} < 0$  now only at 32.2%, a moderate preference for positive values.<sup>3</sup> Further bandwidth reduction does not modify the  $\chi_{\text{eff}}$  posterior substantially (solid dark pink). These results indicate that it is the LLO data between 35 and 40 Hz that are crucial for measuring  $\chi_{\text{eff}}$ , coinciding with the 36 Hz excess power visible in both the original data, Fig. 1, and the glitch subtracted data, Fig. 2.

The second panel from the top of Fig. 2 shows the whitened time-domain reconstructions. We compare signal reconstructions from two analyses with dramatically different  $\chi_{\text{eff}}$  posteriors: the full bandwidth analysis that prefers  $\chi_{\text{eff}} < 0$  against the  $f_L = 40$  Hz analysis with a mildly positive  $\chi_{\text{eff}}$ . While the two analyses are conducted on different data subsets, we can still evaluate the waveforms across the same times and plot them together. The reconstructions are consistent during the merger (corresponding to high frequencies included in both analyses), but start diverging 2–3 cycles before merger. By eye, the full-band reconstruction better matches the data for  $t \approx -0.6$  s, corresponding to the 36 Hz excess power. When that power is included in the analysis, the signal model absorbs it by setting  $\chi_{\text{eff}} < 0$  and pushing the GW cycle to earlier times. If that power is not part of the analysis,  $\chi_{\text{eff}}$  is no longer required to be negative and the 36 Hz excess power is left unaccounted for.

This conclusion raises the question of whether the 36 Hz excess power is part of the signal or part of a glitch that remained unsubtracted. Though the shift in the  $\chi_{\text{eff}}$  posterior is suggestive of anomalous noise, it is possible that it is at least partly due to loss of information as 6% of  $\rho^2$  in LLO is contained in the 35–40 Hz frequency band. In Sec. III C we contextualize this  $\chi_{\text{eff}}$  shift with simulated signals.

## B. Tracing inference across times

Having identified the crucial frequencies for  $\chi_{\text{eff}}$  inference, here we do the same across time with the time-domain analysis described in Sec. II A 2. When used on the full dataset, frequency- and time-domain analyses should yield equivalent results. Indeed, we find consistent posteriors for  $\chi_{\text{eff}}$  when analyzing GW191109 in the

<sup>3</sup> Since the  $\chi_{\text{eff}}$  prior is centered at zero, this shift to mildly positive values goes beyond regression to the prior. We attribute this to a mild  $\chi_{\text{eff}} - D_L$  degeneracy that arises for merger-only signals. The uniform-in-volume prior favors larger  $D_L$  and results in larger  $\chi_{\text{eff}}$  to compensate for the amplitude reduction. This degeneracy is less pronounced when the signal inspiral is visible, as then  $\chi_{\text{eff}}$  is constrained by the inspiral phase evolution beyond just the merger amplitude.

frequency and time domains, as seen by the solid histograms in Fig. 2.<sup>4</sup>

However, as Fig. 1 shows, there is no 1-to-1 mapping between time and frequency for the glitch. Though not as apparent, the same is true for the signal beyond the inspiral regime or due to spin-precession and higher-order modes. Truncating the data in the time domain is, therefore, not equivalent to truncating in the frequency domain, as the former allows us to probe the effect of individual cycles (or parts of cycles) of the signal or the glitch.

Results from progressively excluding the earlier portion of the signal in the time-domain (Run 10 in Table I) are shown in Fig. 2 (blue shading). We find broadly similar results as the frequency-domain analysis: the full data yield preference for  $\chi_{\text{eff}} < 0$ . As the segment that contains the 36 Hz excess power is progressively removed (blue vertical lines in the top panel), the  $\chi_{\text{eff}}$  posterior shifts to being principally positive (equivalent blue histograms in the bottom panel). Overall, the data 0.1–0.04 s before merger are crucial for  $\chi_{\text{eff}} < 0$  inference. Compared to the frequency-domain results, the shift in the  $\chi_{\text{eff}}$  posterior is more gradual, likely due to the fact that the 36 Hz power is more concentrated in frequency, hence no time “cut” abruptly completely excludes it. Waveform reconstructions from the time-domain analysis (third panel from the top in Fig. 2) yield consistent conclusions.

## C. Simulated signals

We investigate the degree to which the abrupt shift in the  $\chi_{\text{eff}}$  posterior in Fig. 2 is consistent with SNR loss from removing data with simulated signals. We simulate 100 signals drawn from the GW191109 full-band posterior (Run 1 in Table I), add them to Gaussian noise drawn from the GW191109 PSDs in LLO and LHO, and analyze the full data versus the  $> 40$  Hz data in LLO independently (Runs 22–221 in Table I). Signals have true values  $\chi_{\text{eff}} < 0$  but as data and signal SNR are removed when  $f_L = 40$  Hz, we expect the posterior to become more prior-like and shift toward  $\chi_{\text{eff}} = 0$ . For each simulated signal, Fig. 3 shows the probability of  $\chi_{\text{eff}} \leq 0$

<sup>4</sup> The time- and frequency-domain analyses employ different priors on masses, luminosity distance, and time. The time-domain inference uses priors which are uniform in detector-frame total mass, mass ratio, and luminosity distance; and are normally distributed in geocenter time, centered at 1257296855.2114642 with a width of 0.005 seconds. We confirm that the differences in time and the mass priors effect the posteriors minimally. Reweighting between the two luminosity distance priors proves difficult due to finite sampling and upweighting portions of parameter space with no support in the posterior. However, the luminosity distance posteriors from the time- and frequency-domain analyses are in high agreement when the full data is analyzed, despite using different priors.



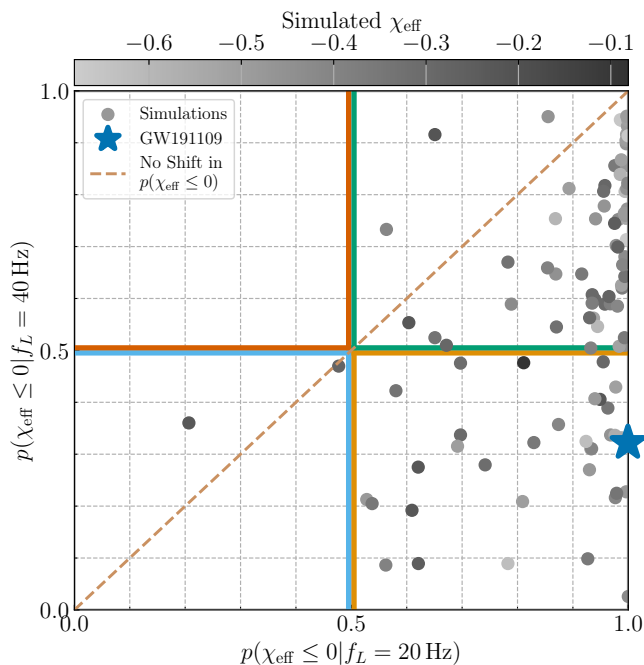


FIG. 3. Shifts in the probability of  $\chi_{\text{eff}} \leq 0$  for 100 simulated signals consistent with GW191109 in Gaussian noise (dots) and the real signal (cross). The x-axis corresponds to a full-band analysis, while the y-axis corresponds to a restricted-band analysis with  $f_L = 40$  Hz. Going clockwise, the top left quadrant (red-orange axes) would contain cases where the posterior shifted from majority positive to negative (of which there were none), the top right quadrant (green axes) contains cases which were majority negative in both full- and restricted-band analyses, the bottom right quadrant (orange axes) contains cases which started majority negative and became majority positive (including GW191109), and the bottom left quadrant (blue axes) contains cases which were consistently majority positive. The  $x = y$  line (dashed brown) corresponds to no shift in the probability for  $\chi_{\text{eff}} \leq 0$ .

from the full-data,  $f_L = 20$  Hz, and the restricted-data,  $f_L = 40$  Hz, analysis.

For almost all signals removing low-frequency LLO data results in a  $\chi_{\text{eff}}$  posterior that shifts closer to the prior and positive values (lying below the diagonal) as expected for signals with true values of  $\chi_{\text{eff}} < 0$ . In most cases, this shift is marginal, and posteriors stay majority-negative, as evidenced by the high density (64% of all signals) in the top right quadrant (green axes). The next most likely outcome is the bottom right quadrant (orange axes), which contains 34% of the signals, including GW191109: here the  $\chi_{\text{eff}}$  posterior shifts from favoring negative to positive values. Among these, GW191109 is one of the more extreme cases, exhibiting a shift more significant than 94% of the simulations. Therefore, we conclude that the  $\chi_{\text{eff}}$  shift presented in Fig. 2 is *unlikely*, but not impossible, to be explained by a random Gaussian noise instantiation, i.e. without needing to invoke residual glitch power. In App. E we present fur-

ther results based on a  $\chi^2$  test used in search algorithms that tracks how SNR is accumulated along the signal [60–62]. Consistent with Fig. 3, the test is inconclusive: the full-band analysis (Run 1 in Table I) has behavior more extreme than most simulations, but it is not strongly inconsistent with them.

#### IV. GLITCH-MARGINALIZED INFERENCE

Having established that the 35–40 Hz data drive the negative  $\chi_{\text{eff}}$  inference, we turn to the question of whether these data are meaningfully impacted by residual glitch power. We go beyond subtracting a single estimate for the glitch and simultaneously model both the signal and the glitch as described in Sec. II C 3. All analyses in this section use the original data in both detectors with no prior glitch mitigation. While this approach is robust against residual glitch power from subtracting a single glitch estimate, it is still impacted by modeling choices, specifically both the parametrized model (physical scattering model or wavelets) and the corresponding glitch parameter priors.

Since the 36 Hz excess power coincides in frequency with an arch predicted by the witness channel, Fig. 1, it is reasonable to expect it to be part of the scattering event and thus a prime target for the slow scattering model [29]. However, the time-frequency morphology of the 36 Hz excess power does not resemble scattering arches, which motivates the alternative wavelet-based glitch model. In principle, BAYESWAVE can fit any excess power by adding enough wavelets. Such a many-wavelet fit might be statistically disfavored, though, as it relies on a large number of parameters and a reduced posterior-to-prior volume. The exact quantitative impact of this Occam penalty is controlled by the wavelet parameter priors, which influence whether it is statistically favorable to add a wavelet to capture the excess power or instead attribute it to the signal. The most influential prior is likely the one for the wavelet amplitude, which —although broad— favors wavelets with  $\text{SNR} \sim 5$ . The situation is further complicated by the low LHO sensitivity in the relevant frequencies, which weakens its contribution to the likelihood, making the discrimination between glitch and signal even more dependent on the prior shape.

##### A. Slow scattering glitch model

We begin with the scattered light model in Fig. 4 (Run 13 in Table I), which models five arches with a uniform amplitude prior and the “Targeted” modulation prior that is informed by the witness motion. The signal is modeled with NRSUR7DQ4. The top panel shows a spectrogram of the data and the signal and glitch posteriors. The inferred glitch arches (multiple colors) match the witness prediction for the arch peak fre-

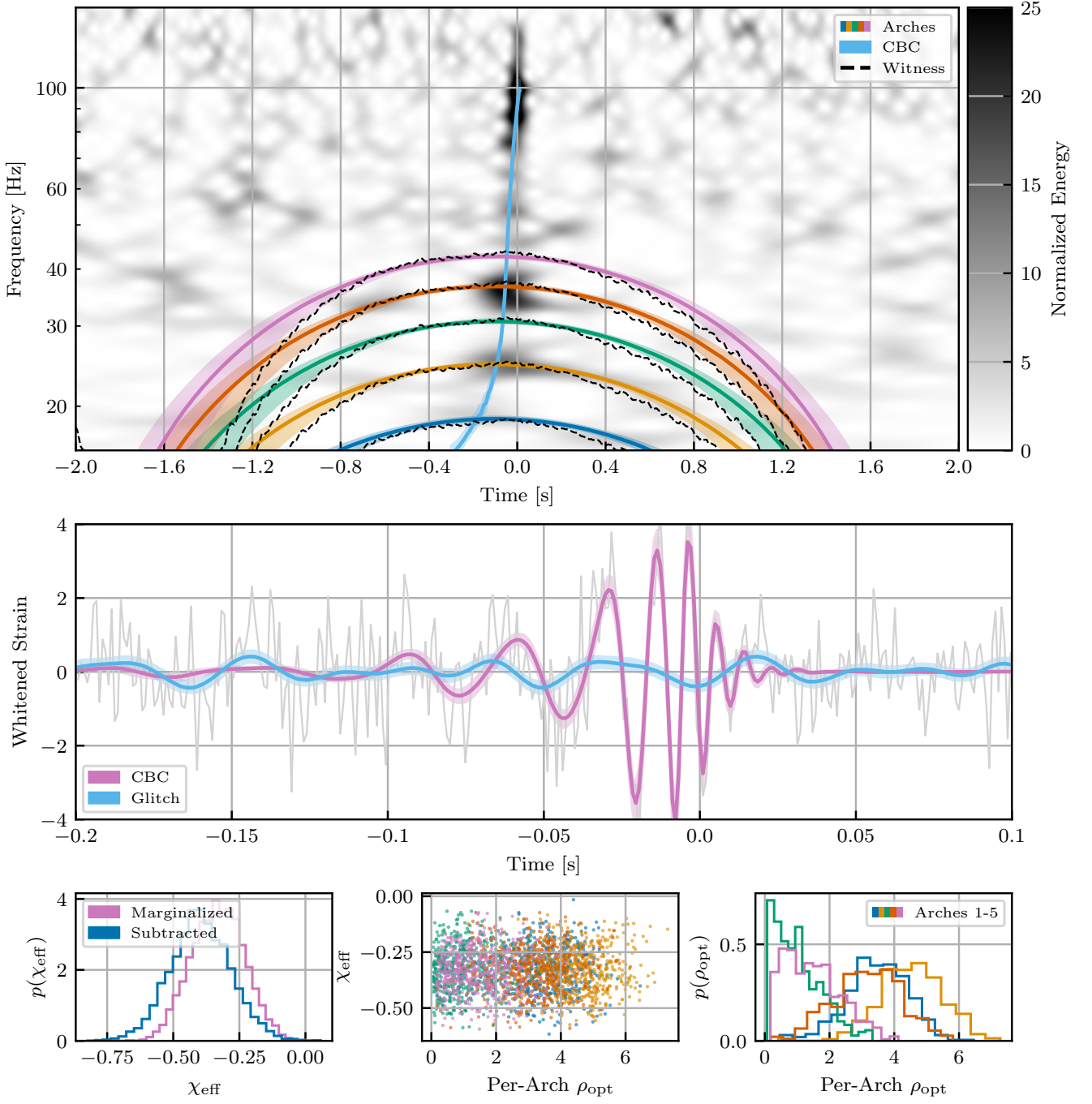


FIG. 4. Jointly modeling the glitch with the physical slow scattering model and the signal with NRSUR7DQ4 (Run 13 in Table I). In the top panel, we show a spectrogram of the data, along with the posterior for the glitch arches (median and 90% credible intervals; multiple colors), the signal track (blue), and the prediction of the witness channel (black dashed). In the middle panel, we show the whitened time-domain posterior reconstruction for the glitch (blue) and the signal (CBC; pink). In the bottom left panel, we show the marginalized  $\chi_{\text{eff}}$  posterior from this analysis (pink), along with the equivalent result from glitch-subtracted data (Run 1 in Table I; blue). In the bottom right panel, we show the marginalized posterior for the optimal SNR of each individual arch. Finally, in the bottom middle panel, we show a scatter plot of individual posterior samples in the  $\rho_{\text{opt}} - \chi_{\text{eff}}$  plane for each arch, showing that no correlation exists.

quency spacing ( $\sim 6$  Hz) in the region of maximum glitch power. The optimal SNR  $\rho_{\text{opt}}$  posterior for each arch is shown in the bottom right panel, which reveals that three non-consecutive arches are confidently recovered with  $\rho_{\text{opt}} > 0$ : the first one at 18 Hz (blue), the second at 24 Hz (yellow), and the fourth at 36 Hz (orange). The third arch at 30 Hz has negligible SNR,  $\rho_{\text{opt}} < 2$  at 88% credibility. Though seemingly surprising given the physical interpretation of scattered light based on bounces off of moving surfaces, a varying arch amplitude is commonly observed and the SNR further depends on the noise PSD that decreases with frequency in this range. The full glitch reconstruction in the time domain is plotted in the middle panel (blue) along with the signal (pink). As expected from the presence of multiple arches, the glitch does not have a constant frequency.

The  $\chi_{\text{eff}}$  inference is presented in the bottom row. The bottom left panel shows the marginalized  $\chi_{\text{eff}}$  posterior from this analysis (pink). For comparison, we also plot the posterior from the standard two-step analysis where the glitch has been pre-subtracted and only the signal is analyzed (Run 1 in Table I; blue). Under glitch marginalization,  $\chi_{\text{eff}}$  remains definitively negative at  $\sim 100\%$  credibility, though the median increases from  $-0.40$  to  $-0.33$ . The glitch and  $\chi_{\text{eff}}$  inference are uncorrelated, as shown in the bottom middle panel through a scatter plot for  $\chi_{\text{eff}}$  and the optimal SNR of each arch.<sup>5</sup> This suggests that even though there is a glitch arch at 36 Hz its time-frequency morphology does not match the 36 Hz excess power. Even when the signal and glitch are simultaneously modeled, most of the 36 Hz excess power is attributed to the signal and results in  $\chi_{\text{eff}} < 0$ . The time-domain reconstructions in the middle panel confirm this interpretation, with the signal reconstruction closely resembling those in Fig. 2, while a lower-amplitude glitch oscillation accounts for the remainder. We have verified that these  $\chi_{\text{eff}}$  results are robust under alternative, yet reasonable, priors for the glitch: log-uniform in amplitude and the ‘‘Physical’’ modulation prior discussed in Sec. IIB 1 (Runs 14, 15, and 16 in Table I for uniform amplitude with physical modulation, log-uniform amplitude with targeted modulation, and log-uniform amplitude with physical modulation respectively). We have also verified that other parameters, such as the binary total mass and mass ratio, remain consistent between glitch-subtracted and glitch-marginalized analyses.

To summarize, we conclude that the 36 Hz power is not exclusively due to the signal. Not only does the witness channel predict some glitch power, but also the slow scattering model places an  $\rho_{\text{opt}} \sim 3$  arch, notably louder

than its adjacent arches. However, the excess power is not entirely attributed to scattered light as it is morphologically inconsistent with a slow scattering arch.<sup>6</sup> The  $\chi_{\text{eff}} < 0$  inference, therefore, persists under the physical slow scattering interpretation of this glitch.

## B. Wavelet glitch model

The physically-motivated slow scattering model finds some glitch power at 36 Hz but cannot account for the entire 36 Hz excess power. This might be because of modeling systematics, the presence of other (beyond slow-scattering) non-Gaussian noise, or simply because the 36 Hz excess power is indeed part of the signal. We explore these possibilities with BAYESWAVE and its more flexible wavelet-based glitch model as described in Sec. IIB 2. We present two analyses: both marginalize over the glitch with wavelets but the GW signal is modeled with either the compact binary model IMRPHENOMXPHM or with coherent wavelets.

### 1. IMRPHENOMXPHM

In Fig. 5 we show results from the joint analysis with IMRPHENOMXPHM for the signal and wavelets for the glitch (Run 21 in Table I). The top panel shows the whitened time-domain reconstructions. Compared to the reconstructions in Fig. 4 there is now increased uncertainty around the 36 Hz excess power, i.e. between times  $-0.09$  and  $-0.04$  s. This is due to the larger flexibility of the glitch model, which can now compete with the signal for the data around  $-0.06$  s, leading to larger uncertainties for both models. The larger uncertainty is also reflected in the glitch-marginalized  $\chi_{\text{eff}}$  posterior shown in the bottom right panel. Compared to Fig. 4, the  $\chi_{\text{eff}}$  posterior is now much wider and entirely consistent with zero. It displays a broadly bimodal structure with one mode favoring  $\chi_{\text{eff}} < 0$  and peaking at  $\sim -0.4$  and the other favoring  $\chi_{\text{eff}} > 0$  and peaking at  $\sim 0.4$ . The anti-aligned mode is weakly favored at 70% of the posterior samples have  $\chi_{\text{eff}} < 0$ .

The increased  $\chi_{\text{eff}}$  uncertainty is entirely due to the glitch and the competition between the signal and the glitch models. The bottom middle panel shows a posterior scatter plot for  $\chi_{\text{eff}}$  and the SNR of the glitch in LIGO Livingston.<sup>7</sup> The glitch SNR is strongly correlated

<sup>5</sup> Rather than the 36 Hz power, we attribute the small shift in the  $\chi_{\text{eff}}$  median in Fig. 4 to the particular glitch realization that was subtracted for the GWTC-3 analysis. Indeed when we analyze the original data (no glitch mitigation) with only a signal (Run 12 in Table I), we obtain a  $\chi_{\text{eff}}$  posterior more similar to that of the marginalized analysis with a median  $\chi_{\text{eff}}$  of  $-0.36$ .

<sup>6</sup> In App. D we show that unphysical priors on the slow scattering parameters can indeed twist the model into fully absorbing the 36 Hz power and eliminating the  $\chi_{\text{eff}} < 0$  inference. Such priors are, however inconsistent with slow scattering, which forms the basis of the glitch model to being with.

<sup>7</sup> This analysis allows for glitches in both detectors, but the Hanford data are consistent with no glitch power in the analysis window.

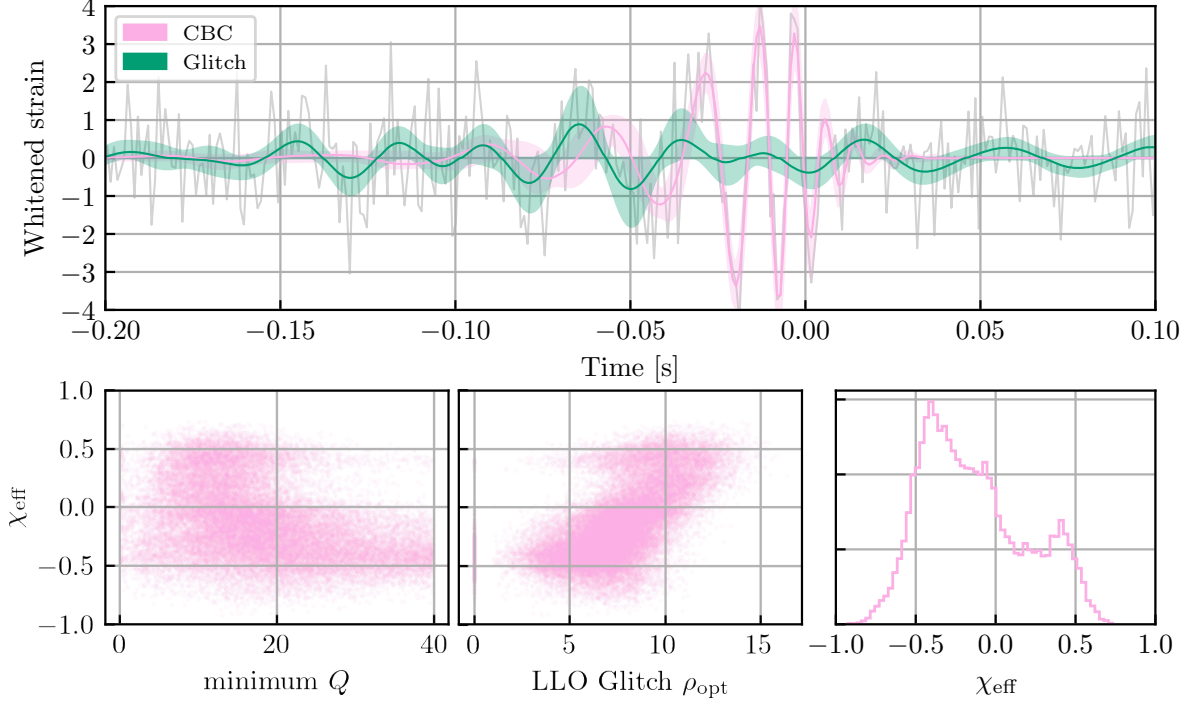


FIG. 5. Jointly modeling the glitch with sine-Gaussian wavelets and the signal with IMRPHENOMXPHM (Run 21 in Table I). The top panel shows the whitened time-domain data (grey) and median and 90% credible intervals for the glitch (green) and signal (CBC; pink). The bottom row displays marginalized posteriors. The right panel shows the glitch-marginalized  $\chi_{\text{eff}}$  posterior, which displays a much larger spread than the results of Fig. 4, now being consistent with  $\chi_{\text{eff}} = 0$ . The left panel shows the scatter plot between  $\chi_{\text{eff}}$  and the minimum quality factor  $Q$  among all wavelets of each posterior sample. Positive  $\chi_{\text{eff}}$  is correlated with low  $Q$ . Scattered light is characterized by larger  $Q$ -values [34], confirming that  $\chi_{\text{eff}} > 0$  only if the glitch does not match the expected scattered light morphology. The middle panel shows a scatter plot between  $\chi_{\text{eff}}$  and the glitch SNR which are again correlated: higher glitch power leads to a more positive  $\chi_{\text{eff}}$ .

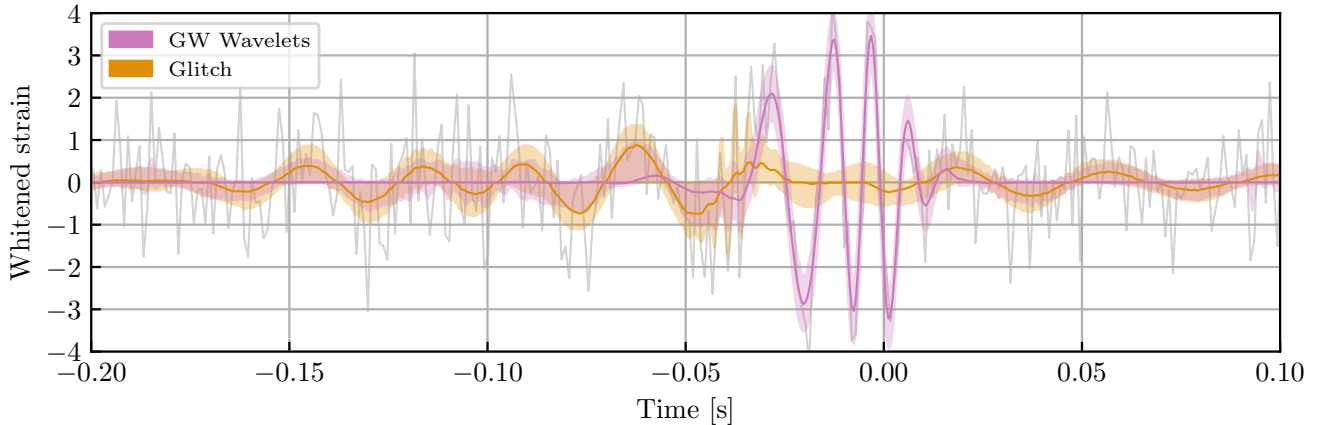


FIG. 6. Jointly modeling both the glitch and the signal with sine-Gaussian wavelets (Run 20 in Table I). We plot the whitened time-domain data (grey) and median and 90% credible intervals for the glitch (orange) and signal (GW Wavelets; purple). The 36 Hz excess power is consistent with originating from either the glitch or the signal at the 90% credible level.

with  $\chi_{\text{eff}}$ : a higher glitch power results in a more positive  $\chi_{\text{eff}}$ . A small fraction of posterior samples,  $\sim 6\%$ , have vanishing glitch SNR (zero wavelets) and a strongly negative  $\chi_{\text{eff}}$ , consistent with results from Fig. 4. Besides the glitch power, we examine the recovered glitch morphology in the bottom left panel, where we plot  $\chi_{\text{eff}}$  against the minimum quality factor among wavelets in a particular posterior sample. The quality factor corresponds to the number of cycles in a wavelet, therefore scattering arches are characterized by larger values of  $Q$  [34]. This plot confirms the conclusions of Fig. 4: if the glitch is scattering-like (large  $Q$ ), the model cannot capture the 36 Hz power, and  $\chi_{\text{eff}}$  tends to be negative. Support for  $\chi_{\text{eff}} > 0$  requires low values of  $Q$  which morphologically do not resemble scattering arches.

These results are qualitatively robust against different glitch priors. When using a prior for the amplitude of each wavelet that peaks at an SNR of 3 (instead of the default value of 5), we recover the same bimodal solution for  $\chi_{\text{eff}}$  and the glitch SNR. However, the preference for the antialigned mode shifts from 70% to 60% suggesting that our quantitative results are impacted by the glitch prior at the few percent level. This shift is attributed to the fact that the updated prior makes it easier to low-SNR wavelets to be added to the posterior and thus capture the 36 Hz excess power away from the signal model. The impact of glitch priors is akin to the impact of compact-binary parameters on inference [63] and is expected to be more prominent for low-SNR glitches.

We perform a final sanity check by comparing the total (signal plus glitch) reconstructions of posterior samples with  $\chi_{\text{eff}} > 0$  to those with  $\chi_{\text{eff}} < 0$ . Although the two posterior modes result in different interpretations of which parts of the data are signal and which are glitch, their sums are consistent with each other. This is expected as it is the total strain of signal-plus-glitch that is compared to the data to calculate the likelihood. So any solution must result in the same total strain. While we view this as a sanity check on the analysis convergence, it also suggests that there are 2 distinct ways to model the data, and this analysis does not strongly prefer one over the other.

## 2. Coherent wavelet model

For completeness, we present a final analysis where both the glitch and the GW are modeled with sums of wavelets [35] (Run 20 in Table I). Since the signal model is now also phenomenological, we do not extract any binary parameters such as  $\chi_{\text{eff}}$  which has thus far been guiding our conclusions. Instead, we directly interpret the time-domain reconstructions in Fig. 6. As expected, using more flexible models results in increased uncertainties. The 36 Hz ( $-0.06$  s in the plot) power is still traded between the two models, and neither can rule out that it belongs to them at the 90% credible level. In contrast to the signal reconstructions thus far, Figs. 4 and 5, the

coherent wavelet model is not able to confidently recover the signal inspiral between times  $-0.1$  and  $-0.04$  s. This is again due to the large flexibility of the wavelet signal model, which needs to extract each portion of the signal independently of the others [64] as opposed to the waveform model that coherently models the whole signal across inspiral and merger.

## C. Comparing glitch reconstructions

Finally, we compare glitch reconstructions from the various glitch inferences considered in Fig. 7. The comparison includes the single glitch realization considered in GWTC-3 [1] and the three glitch-marginalized analyses presented in this study, Figs. 4, 5, and 6. The glitch reconstructions are largely consistent with each other, with the largest differences encountered in the crucial  $-0.06$  s region. As expected, the wavelet-based reconstructions have a larger statistical uncertainty due to the larger model flexibility. This allows them to reach a larger amplitude at  $-0.06$  s which is necessary in order to capture the 36 Hz excess power.

## V. CONCLUSIONS

When seeking to interpret GW data in the presence of glitches, absolute confidence in all aspects of the analysis is impossible. Unlike compact-binary signals for which we have exact numerical relativity simulations to compare models against, glitch modeling does not have the luxury of a “ground truth” solution. Nonetheless, we have sought an understanding of GW191109, its astrophysically-influential  $\chi_{\text{eff}} < 0$  inference, and the overlapping glitch within the limitations of imperfect glitch models and large statistical uncertainties.

We showed that the  $\chi_{\text{eff}} < 0$  measurement is attributed to a segment of LIGO Livingston data occurring between 0.1 and 0.04 s before the merger, and between 30 and 40 Hz. These data are impacted by excess scattered light non-Gaussian noise, consistent with Ref. [28]. Simultaneously modeling the GW signal with compact-binary waveforms and the glitch yields results that depend on the glitch model. A physical glitch model tailored to slow scattering glitches cannot morphologically match the excess power observed in the 36 Hz range. Therefore the  $\chi_{\text{eff}} < 0$  measurement still stands. A more flexible wavelet-based glitch model is instead able to fully account for the 36 Hz excess power and wipe out all support for  $\chi_{\text{eff}} < 0$ . Though witness channel information suggests that slow scattering was indeed what occurred during GW191109, we cannot rule out shortcomings of the slow scattering parametrized model or additional non-Gaussian noise.

Given this, we cannot make absolute statements about the properties of GW191109. If, as expected from witness channel information, the data contain Gaussian noise,

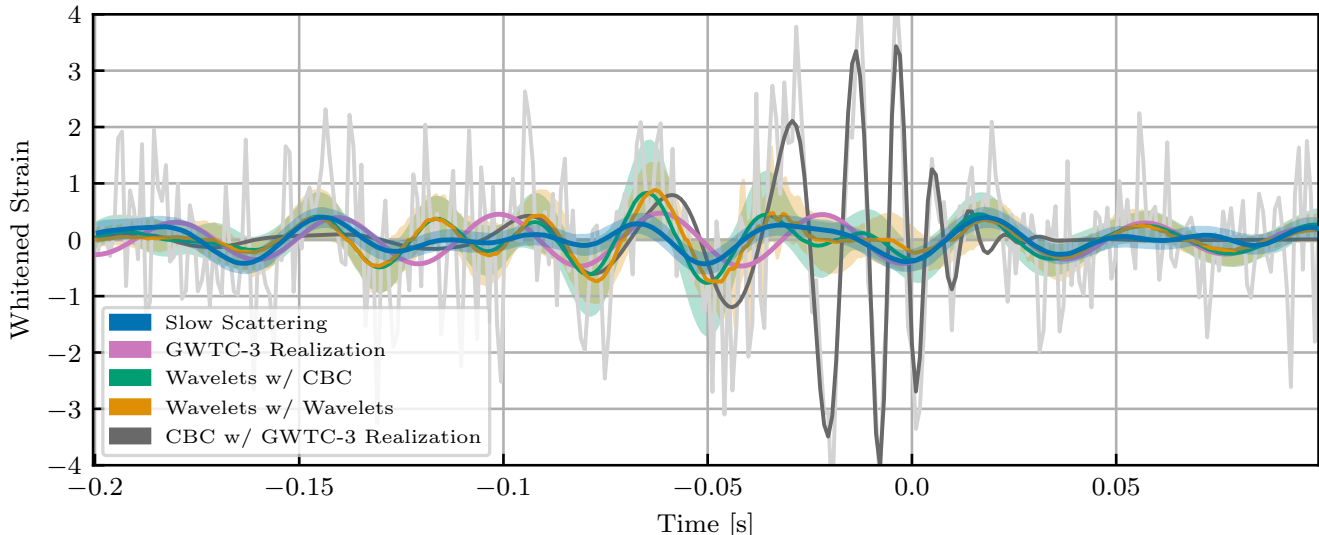


FIG. 7. Comparison of reconstructions for the LIGO Livingston glitch that overlapped with GW191109 obtained by various analyses. The data are shown in grey, and for reference, we also show the maximum-likelihood GW reconstruction from the full-band analysis on the glitch-subtracted data in black (Run 1 in Table I). The single realization subtracted for the GWTC-3 analysis is shown in pink [1]. The glitch inferred from the joint slow scattering and NRSUR7DQ4 analysis (Run 13 in Table I) is shown in blue. The glitch inferred with wavelets is shown in green when the signal is modeled with IMRPHENOMXPHM (Run 21 in Table I) and orange when the signal is also modeled with wavelets (Run 20 in Table I).

a well-modeled slow scattering glitch, and a GW signal, then GW191109 likely had asymmetric masses and  $\chi_{\text{eff}} < 0$ , strongly implying a dynamical origin [8]. However, if other non-Gaussian noise was present in the data, or the glitch morphology varied from classical slow scattering, spin inference becomes uninformative — though in any situation, GW191109 remains one of the heaviest observations to date. Distinguishing between these interpretations is challenging. Firstly, LIGO Hanford’s sensitivity in the relevant frequency range is diminished, it can therefore not contribute to the question of whether the crucial 36 Hz power is coherent (and thus part of the signal) or incoherent (and thus part of the glitch). Secondly, the overall low SNR of the glitch makes results depend on the glitch model priors, e.g. the BAYESWAVE glitch prior explored in Sec. IV B.

Our analysis builds upon Refs. [28, 33] to propose a framework for in-depth analyses of glitch-afflicted data. The framework includes cross-detector comparisons, band- and time-limited analyses, simulated signals, marginalizing over the glitch, and exploring different glitch models (tailored to a specific glitch family or flexible) and prior assumptions.

As GW astronomy collects more data and seeks to constrain increasingly more subtle effects, mitigating systematics related to data quality presents a complementary challenge to waveform systematics. Similar to waveform systematics, data quality systematics can be particularly troublesome for spin inference, which typically leaves a subtle imprint on the data and is concentrated on a small (time or frequency) region of data. Studies such as the

ones presented here and in Ref. [33] are based on targeted, intensive follow-up of selected events, hand-chosen for the astrophysically important inference. Data quality systematics aggregating over catalogs of detections require additional care to identify and mitigate in an automated way, e.g., [65]. Such efforts will be significantly aided by the work of experts in reducing the absolute rate of glitches, in characterizing the state of the detectors, and in developing efficient and statistically sound analyses in the presence of glitches. In this work we present techniques to help address these challenges moving forward.

## ACKNOWLEDGMENTS

We thank Jess McIver, Niko Lecoche, Eric Thrane, Paul Lasky, Hui Tong, Maya Fishbach, Ethan Payne, and Jacob Golomb for helpful discussions about this analysis. We thank Lucy Thomas and Aaron Zimmerman for insightful discussions on the behavior of merger dominated waveforms and the  $\chi_{\text{eff}} - D_L$  degeneracy. We thank Isobel Romero-Shaw and Tousif Islam for assistance with accessing and interpreting previous analyses. We thank Colm Talbot for assistance in the implementation of glitch inference in BILBY. We thank Carl-Johan Haster for helpful comments on the manuscript.

RPU and DD are supported by NSF Grant PHY-2309200. SM, SH, HD, and KC were supported by NSF Grant PHY-2110111 and NSF Grant PHY-2308770. SH was supported by the National Science Foundation Graduate Research Fellowship under Grant DGE-1745301.

This work was partially supported by the generosity of Eric and Wendy Schmidt by recommendation of the Schmidt Futures program. The Flatiron Institute is funded by the Simons Foundation.

This material is based upon work supported by NSF’s LIGO Laboratory which is a major facility fully funded by the National Science Foundation. LIGO was constructed by the California Institute of Technology and Massachusetts Institute of Technology with funding from the National Science Foundation, and operates under cooperative agreement PHY-2309200. The authors are grateful for computational resources provided by the LIGO Laboratory and supported by National Science Foundation Grants PHY-0757058 and PHY-0823459.

This work made use of NUMPY [66], SCIPY [67], MATPLOTLIB [68], LALSUITE [69], DYNESTY [44], GWPY [70], ASTROPY [71], BILBY [20], BILBY\_PIPE [21], PYCBC [72], GWDETCAR [73], and BAYESWAVE [37–39].

### Appendix A: Scattered light glitches in LHO

In Fig. 8 we show a spectrogram of the data in LHO at the time of GW191109 and the scattering tracks predicted by the witness channel. When GW191109 entered the LHO frequency band, the scattering surface motion was at a minimum, so that the signal and the glitch are disjoint in time and frequency. Accordingly, we expect source inference to be unaffected by the glitch. Reference [28] reached similar conclusions. We confirm this expectation by performing analyses which restrict the frequency band in LHO in a similar fashion to main-text LLO analyses. When restricting to  $> 40$  Hz in LHO (Run 6 in Table I) but with no LLO restrictions, the  $\chi_{\text{eff}}$  posterior remains almost entirely negative ( $\chi_{\text{eff}} < 0$  at 99.9% credibility, the same as Run 1 in Table I that uses all data in both detectors). When removing sub-40 Hz data in both detectors (Run 7 in Table I), we obtain a modestly positive result ( $\chi_{\text{eff}} < 0$  at 33.3% credibility), but no more so than when we only restricting the LLO data (32.2%) (Run 4 in Table I). While it is mildly surprising that removing so much low-frequency data in LHO has so little apparent effect on inference, we attribute this to the significant difference between LLO and LHO low-frequency sensitivity.

### Appendix B: Detailed analysis settings

In this Appendix we provide details about the settings of all analyses presented in this study. Table I identifies all analyses with a unique index, referenced throughout the text. We also list the data analyzed, the relevant glitch and signal models, any restrictions applied to the data being analyzed, and the analysis type (both the software used and the data domain in which it operates). Data for these analyses is made public in the associated zenodo dataset [75].

### Appendix C: IMRPhenomXPHM Analyses with bilby

To assess whether differences between BAYESWAVE results and BILBY results are due to waveform systematics, we also perform two analyses using BILBY and IMRPHENOMXPHM: one on subtracted data (Run 11 in Table I), and one using the slow scattering glitch model (Run 19 in Table I). The analysis on subtracted data found  $\chi_{\text{eff}} \leq 0$  at 99.3% credibility, while the analysis marginalizing over the slow scattering model found  $\chi_{\text{eff}} \leq 0$  at 99.9% credibility. From this we conclude that the observed differences between BILBY and BAYESWAVE are due to the choice of glitch model, rather than the choice of waveform approximant.

### Appendix D: Alternate Slow Scattering Glitch Priors

To test our assumption that it is appropriate to use the slow scattering model with five scattering arches, we also perform a test using four scattering arches with uniform amplitude and targeted modulation frequency priors (Run 17 in Table I). This result finds  $\chi_{\text{eff}} \leq 0$  with  $\sim 100\%$  credibility, indicating that the inclusion of an arch around 42 Hz does not alter the conclusions of this work.

The slow scattering model under the physically expected range of modulation frequencies  $f_{\text{mod}} \sim \mathcal{U}(0.05 - 0.3)$  Hz results in arches that are too extended in time to match the 36 Hz excess power morphology. We explore what values of  $f_{\text{mod}}$  are required in order to impact  $\chi_{\text{eff}}$  inference, with an analysis that employs a uniform amplitude prior and a maximum modulation frequency of 5 Hz (Run 18 in Table I). We recover a tri-modal structure favoring  $f_{\text{mod}} = 1.5$  Hz and a less negative  $\chi_{\text{eff}}$ , with  $\chi_{\text{eff}} < 0$  at 77.1% credibility. However,  $f_{\text{mod}} = 1.5$  Hz is 10 times larger than the scattering surface motion witnessed by the channel L1:SUS-ETMX.L2.WIT.LDQ. Such a result would presume the existence of some alternative source of frequency modulated phase noise, either due to another scattering surface driven at a different frequency, or some non-scattering mechanism, coincidentally aligned in time and frequency with the known scatterer. While we cannot rule out the existence of such a source, there is no physical motivation to presuppose its existence. We instead use this analysis to emphasize the conclusion from the BAYESWAVE study, namely that sufficiently flexible glitch models allow for a wider range of possibilities.

### Appendix E: Frequency Bin $\chi^2$ Test

Tests which assess the Gaussianity of data [76, 77] may be applied to residual data after glitch and signal subtraction, but these do not address whether the signal model is

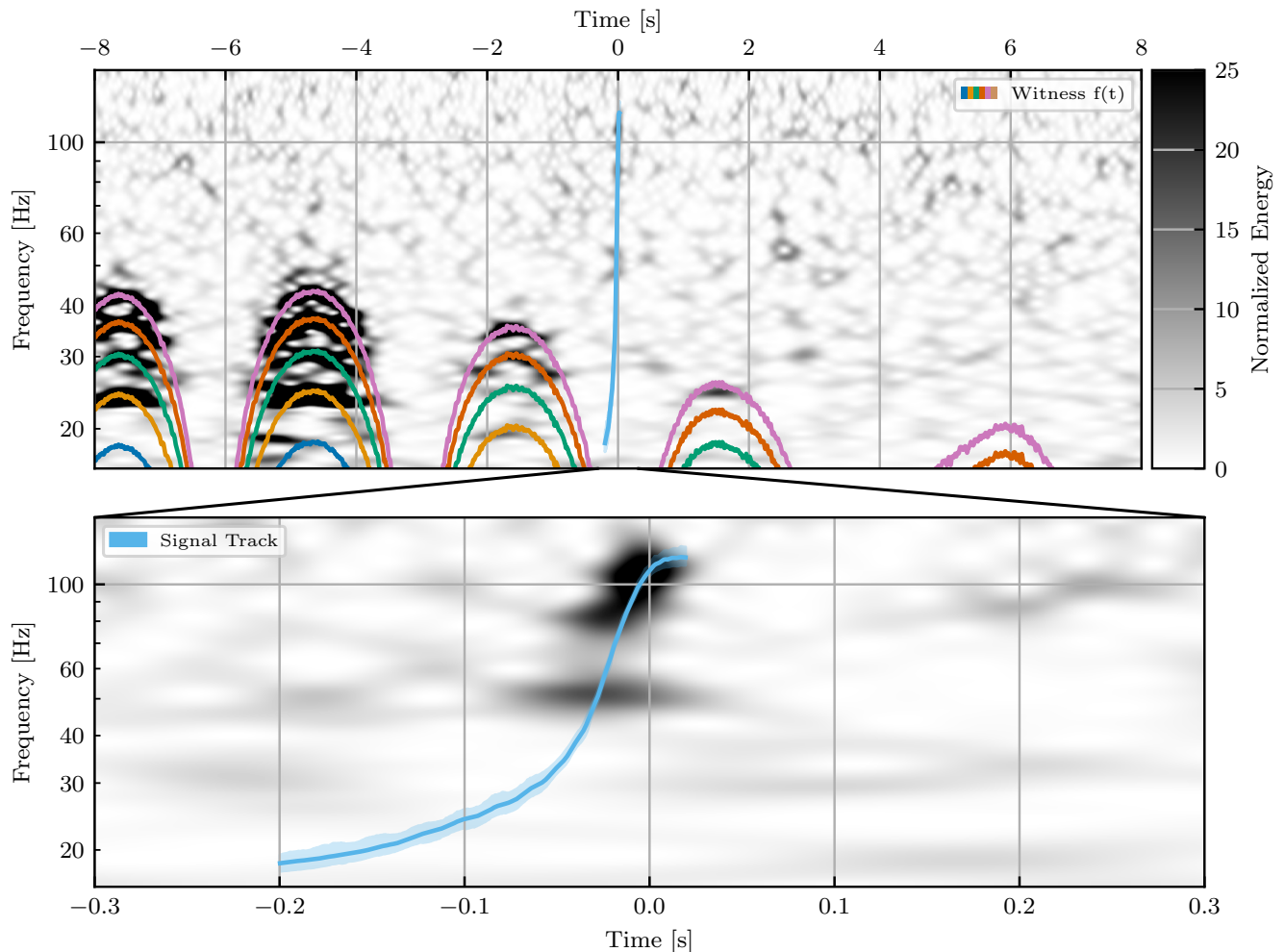


FIG. 8. Similar to Fig. 1 but for LHO data at the time of GW191109, with the scattering tracks predicted by the motion of the witness channel H1:SUS-ETMX.L2.WIT.L.DQ. The absolute intensity of the slow scattering was significantly worse than in LLO, but the signal occurred at a minimum in the scattering, such that there is no overlap in time and frequency between the glitch arches and the GW191109 track (blue).

capturing any glitch power. In this Appendix we instead consider the frequency bin  $\chi^2$  test as employed by search algorithms [60–62]. Qualitatively, it assesses tension between the signal waveform and the data over the entire frequency band, and hence measures deviations due both to model misspecification and to distribution of power not characteristic of a CBC, e.g., a glitch.

For each posterior waveform, we divide the frequency band into  $p$  bins of equal optimal SNR. If the data are consistent with the sum of the waveform in question and Gaussian noise, then the matched-filter SNR will also be evenly distributed over these bins. For the  $j$ th bin, the matched-filter SNR  $\rho_{\text{mf},j}$  will deviate from the mean  $\rho_{\text{mf}}$

$$\Delta\rho_{\text{mf},j} = \rho_{\text{mf},j} - \frac{\rho_{\text{mf}}}{p}. \quad (\text{E1})$$

The statistic

$$\chi^2 = p \sum_{j=1}^p |\Delta\rho_{\text{mf},j}|^2, \quad (\text{E2})$$

is distributed according to a  $\chi^2$  distribution with  $2p - 2$  degrees of freedom under Gaussian noise[60].<sup>8</sup> The normalized statistic

$$\chi_r^2 = \frac{\chi^2}{2p - 2}, \quad (\text{E3})$$

will then have an expected value of 1. Deviations indicate that the data might not be solely described by the

<sup>8</sup> Two degrees of freedom correspond to the real and imaginary components in each bin, while two are removed since deviations must sum to zero in each of the real and imaginary components.



Run ID	Data	Glitch Model	Signal Model	Data Restrictions	Analysis Type
1	Subtracted	—	NRSUR7DQ4	—	BILBY-FD
2	Subtracted	—	NRSUR7DQ4	$f_L = 30$ Hz	BILBY-FD
3	Subtracted	—	NRSUR7DQ4	$f_L = 35$ Hz	BILBY-FD
4	Subtracted	—	NRSUR7DQ4	$f_L = 40$ Hz	BILBY-FD
5	Subtracted	—	NRSUR7DQ4	$f_L = 45$ Hz	BILBY-FD
6	Subtracted	—	NRSUR7DQ4	$f_H = 40$ Hz	BILBY-FD
7	Subtracted	—	NRSUR7DQ4	$f_L = f_H = 40$ Hz	BILBY-FD
8	Subtracted	—	NRSUR7DQ4	No LHO	BILBY-FD
9	Subtracted	—	NRSUR7DQ4	No LLO	BILBY-FD
10	Subtracted	—	NRSUR7DQ4	Various $t_H, t_L$	TD
11	Subtracted	—	IMRPHENOMXPHM	—	BILBY-FD
12	Original	—	NRSUR7DQ4	—	BILBY-FD
13	Original	Slow Scattering (Uniform + Targeted)	NRSUR7DQ4	—	BILBY-FD
14	Original	Slow Scattering (Uniform + Physical)	NRSUR7DQ4	—	BILBY-FD
15	Original	Slow Scattering (Log-Uniform + Targeted)	NRSUR7DQ4	—	BILBY-FD
16	Original	Slow Scattering (Log Uniform + Physical)	NRSUR7DQ4	—	BILBY-FD
17	Original	Slow Scattering (Uniform + Targeted, N=4)	NRSUR7DQ4	—	BILBY-FD
18	Original	Slow Scattering (Uniform + Unphysical)	NRSUR7DQ4	—	BILBY-FD
19	Original	Slow Scattering (Uniform + Targeted)	IMRPHENOMXPHM	—	BILBY-FD
20	Original	Wavelets	Wavelets	—	BAYESWAVE-FD
21	Original	Wavelets	IMRPHENOMXPHM	—	BAYESWAVE-FD
22-221	Simulated	—	NRSUR7DQ4	—	BILBY-FD
122-221	Simulated	—	NRSUR7DQ4	$f_L = 40$ Hz	BILBY-FD

TABLE I. Settings and properties for all analyses presented in this work. We list from left to right: a unique run ID hyperlinked in the text, the type of data used (original or glitch-subtracted GWTC-3 data [42, 74]), how the glitch is modeled per Sec. IIB, how the CBC signal is modeled per Sec. IIA, frequency or time cuts on the data on top of the default settings, and the analysis type (software and data domain - FD for frequency and TD for time). Analyses based on glitch-subtracted data use the data provided by GWTC-3 [1], while analyses that marginalize over the glitch employ the original unmitigated data. Frequency bands are described by  $f_H$  and  $f_L$  designating the minimum frequency of analysis in LHO and LLO respectively. For runs which us the parameterized slow scattering model, the parenthetical descriptions correspond to the choice of amplitude prior and modulation frequency prior respectively for each run. All slow scattering analyses model five slow scattering arches, with the exception of Run 17.

waveform plus Gaussian noise, likely due to a glitch. We compute  $\chi_r^2$  for each GW191109 signal posterior sample on data where the corresponding glitch posterior sample has been subtracted. We denote the mean statistic over posterior samples as  $\bar{\chi}_r^2$ . We then compare against corresponding results from the simulated signals of Sec. III C. The reason we compare against simulations rather than directly the frequentist expectation for Eq. (E3) is that the distribution over the posterior samples is not equivalent to a distribution over many Gaussian noise realizations.

In Fig. 9 we plot the statistic distribution over posterior samples in both detectors for the glitch-subtracted analysis of Run 1 and the glitch-marginalized analysis with the slow-scattering model of Run 13. The colormap corresponds to results from simulated signals where we bin the mean statistic  $\bar{\chi}_r^2$  for each simulated signal. Glitch-marginalization results in a statistic whose mean is more closely in accordance with the frequentist expec-

tation value in both detectors ( $\bar{\chi}_r^2 = 0.96$  and  $\bar{\chi}_r^2 = 0.97$  in LHO and LLO respectively) than glitch-subtraction ( $\bar{\chi}_r^2 = 1.16$  and  $\bar{\chi}_r^2 = 1.24$  in LHO and LLO). Compared to the simulated signals, glitch-marginalization results in  $\bar{\chi}_r^2$  more extreme than that of 41% (45%) of simulations in LHO (LLO), while the glitch-subtracted result has a  $\bar{\chi}_r^2$  more extreme than 81% (90%) of simulations in LHO (LLO). To produce a meta-statistic, we use Fisher’s method [78] to compute the likelihood of these statistics occurring together, assuming that the  $p$ -values are uncorrelated. This creates another  $\chi^2$  statistic, this time with two degrees of freedom per detector. For the glitch-marginalized result, we obtain 2.25, corresponding to a  $p$ -value of 0.69, while for the glitch-subtracted results we have 7.93, giving a  $p$ -value of 0.09. Consistent with expectations, glitch-marginalization results in residuals that are more consistent with Gaussian noise after removing the glitch and signal reconstruction.

[1] R. Abbott et al. (KAGRA, VIRGO, LIGO Scientific), Phys. Rev. X **13**, 041039 (2023), arXiv:2111.03606 [gr-

qc].  
[2] E. Racine, Phys. Rev. D **78**, 044021 (2008),

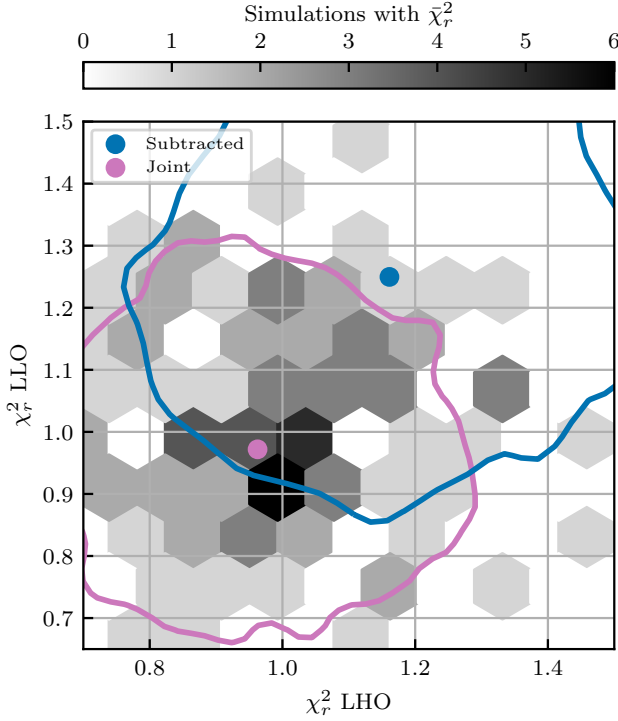


FIG. 9. Distribution of  $\chi_r^2$  in both detectors for the glitch-subtracted analysis (blue; Run 1) and the glitch-marginalized analysis (purple; Run 13). The colormap corresponds to the distribution of  $\bar{\chi}_r^2$  from simulated signals consistent with GW191109, Runs 22-121. Dots denote the distribution mean and contours denote the 90% level. For the reference distribution, we histogram the  $\bar{\chi}_r^2$  values in LHO and LLO from each simulation.

arXiv:0803.1820 [gr-qc].

[3] P. Ajith et al., Phys. Rev. Lett. **106**, 241101 (2011), arXiv:0909.2867 [gr-qc].

[4] L. Santamaria et al., Phys. Rev. D **82**, 064016 (2010), arXiv:1005.3306 [gr-qc].

[5] I. M. Romero-Shaw, P. D. Lasky, and E. Thrane, Astrophys. J. **940**, 171 (2022), arXiv:2206.14695 [astro-ph.HE].

[6] N. Gupte et al., (2024), arXiv:2404.14286 [gr-qc].

[7] A. Antonelli, K. Kritos, K. K. Y. Ng, R. Cotesta, and E. Berti, Phys. Rev. D **108**, 084044 (2023), arXiv:2306.11088 [gr-qc].

[8] R. C. Zhang, G. Fragione, C. Kimball, and V. Kalogera, Astrophys. J. **954**, 23 (2023), arXiv:2302.07284 [astro-ph.HE].

[9] H. Tong, S. Galaudage, and E. Thrane, Phys. Rev. D **106**, 103019 (2022), arXiv:2209.02206 [astro-ph.HE].

[10] C. Adamcewicz, P. D. Lasky, and E. Thrane, Astrophys. J. **958**, 13 (2023), arXiv:2307.15278 [astro-ph.HE].

[11] R. Farmer, M. Renzo, S. E. de Mink, P. Marchant, and S. Justham, (2019), 10.3847/1538-4357/ab518b, arXiv:1910.12874 [astro-ph.SR].

[12] S. E. Woosley and A. Heger, Astrophys. J. Lett. **912**, L31 (2021), arXiv:2103.07933 [astro-ph.SR].

[13] V. Kalogera, Astrophys. J. **541**, 319 (2000), arXiv:astro-ph/9911417.

[14] D. Gerosa, E. Berti, R. O’Shaughnessy, K. Belczynski, M. Kesden, D. Wysocki, and W. Gladysz, Phys. Rev. D **98**, 084036 (2018), arXiv:1808.02491 [astro-ph.HE].

[15] M. Zevin, I. M. Romero-Shaw, K. Kremer, E. Thrane, and P. D. Lasky, Astrophys. J. Lett. **921**, L43 (2021), arXiv:2106.09042 [astro-ph.HE].

[16] I. M. Romero-Shaw, P. D. Lasky, and E. Thrane, Astrophys. J. Lett. **921**, L31 (2021), arXiv:2108.01284 [astro-ph.HE].

[17] P. C. Peters, Phys. Rev. **136**, B1224 (1964).

[18] G. Pratten et al., Phys. Rev. D **103**, 104056 (2021), arXiv:2004.06503 [gr-qc].

[19] S. Ossokine et al., Phys. Rev. D **102**, 044055 (2020), arXiv:2004.09442 [gr-qc].

[20] G. Ashton et al., Astrophys. J. Suppl. **241**, 27 (2019), arXiv:1811.02042 [astro-ph.IM].

[21] I. M. Romero-Shaw et al., Mon. Not. Roy. Astron. Soc. **499**, 3295 (2020), arXiv:2006.00714 [astro-ph.IM].

[22] J. Lange, R. O’Shaughnessy, and M. Rizzo, (2018), arXiv:1805.10457 [gr-qc].

[23] V. Varma, S. E. Field, M. A. Scheel, J. Blackman, D. Gerosa, L. C. Stein, L. E. Kidder, and H. P. Pfeiffer, Phys. Rev. Research. **1**, 033015 (2019), arXiv:1905.09300 [gr-qc].

[24] T. Islam, A. Vajpeyi, F. H. Shaik, C.-J. Haster, V. Varma, S. E. Field, J. Lange, R. O’Shaughnessy, and R. Smith, (2023), arXiv:2309.14473 [gr-qc].

[25] M. Hannam et al., Nature **610**, 652 (2022), arXiv:2112.11300 [gr-qc].

[26] P. Schmidt, F. Ohme, and M. Hannam, Phys. Rev. D **91**, 024043 (2015), arXiv:1408.1810 [gr-qc].

[27] J. Aasi et al. (LIGO Scientific), Class. Quant. Grav. **32**, 074001 (2015), arXiv:1411.4547 [gr-qc].

[28] D. Davis, T. B. Littenberg, I. M. Romero-Shaw, M. Millhouse, J. McIver, F. Di Renzo, and G. Ashton, Class. Quant. Grav. **39**, 245013 (2022), arXiv:2207.03429 [astro-ph.IM].

[29] R. Udall and D. Davis, Appl. Phys. Lett. **122**, 094103 (2023), arXiv:2211.15867 [astro-ph.IM].

[30] F. Acernese (Virgo), J. Phys. Conf. Ser. **610**, 012014 (2015).

[31] C. Pankow et al., Phys. Rev. D **98**, 084016 (2018), arXiv:1808.03619 [gr-qc].

[32] K. Chatziioannou, N. Cornish, M. Wijngaarden, and T. B. Littenberg, Phys. Rev. D **103**, 044013 (2021), arXiv:2101.01200 [gr-qc].

[33] E. Payne, S. Hourihane, J. Golomb, R. Udall, D. Davis, and K. Chatziioannou, Phys. Rev. D **106**, 104017 (2022), arXiv:2206.11932 [gr-qc].

[34] S. Hourihane, K. Chatziioannou, M. Wijngaarden, D. Davis, T. Littenberg, and N. Cornish, Phys. Rev. D **106**, 042006 (2022), arXiv:2205.13580 [gr-qc].

[35] S. Ghonge, J. Brandt, J. M. Sullivan, M. Millhouse, K. Chatziioannou, J. A. Clark, T. Littenberg, N. Cornish, S. Hourihane, and L. Cadonati, (2023), arXiv:2311.09159 [gr-qc].

[36] R. Macas, A. Lundgren, and G. Ashton, Phys. Rev. D **109**, 062006 (2024), arXiv:2311.09921 [gr-qc].

[37] N. J. Cornish and T. B. Littenberg, Class. Quant. Grav. **32**, 135012 (2015), arXiv:1410.3835 [gr-qc].

[38] T. B. Littenberg and N. J. Cornish, Phys. Rev. D **91**, 084034 (2015), arXiv:1410.3852 [gr-qc].

[39] N. J. Cornish, T. B. Littenberg, B. Bécsy, K. Chatziioannou, J. A. Clark, S. Ghonge, and M. Millhouse, Phys.

- Rev. D **103**, 044006 (2021), arXiv:2011.09494 [gr-qc].
- [40] M. Hannam, P. Schmidt, A. Bohé, L. Haegel, S. Husa, F. Ohme, G. Pratten, and M. Pürrer, Phys. Rev. Lett. **113**, 151101 (2014), arXiv:1308.3271 [gr-qc].
- [41] S. J. Miller, M. Isi, K. Chatziioannou, V. Varma, and I. Mandel, “GW190521: tracing imprints of spin-precession on the most massive black hole binary,” (2023), arXiv:2310.01544 [astro-ph.HE].
- [42] R. Abbott et al. (KAGRA, VIRGO, LIGO Scientific), Astrophys. J. Suppl. **267**, 29 (2023), arXiv:2302.03676 [gr-qc].
- [43] R. Abbot et al. (LIGO Scientific Collaboration and Virgo Collaboration and KAGRA Collaboration), “GWTC-3: Compact Binary Coalescences Observed by LIGO and Virgo During the Second Part of the Third Observing Run — Parameter estimation data release,” (2023).
- [44] J. S. Speagle, Mon. Not. Roy. Astron. Soc. **493**, 3132 (2020), arXiv:1904.02180 [astro-ph.IM].
- [45] M. Isi and W. M. Farr, (2021), arXiv:2107.05609 [gr-qc].
- [46] M. Isi, W. M. Farr, M. Giesler, M. A. Scheel, and S. A. Teukolsky, Phys. Rev. Lett. **127**, 011103 (2021), arXiv:2012.04486 [gr-qc].
- [47] M. Isi, M. Giesler, W. M. Farr, M. A. Scheel, and S. A. Teukolsky, Phys. Rev. Lett. **123**, 111102 (2019), arXiv:1905.00869 [gr-qc].
- [48] G. Carullo, W. Del Pozzo, and J. Veitch, Phys. Rev. D **99**, 123029 (2019), [Erratum: Phys.Rev.D 100, 089903 (2019)], arXiv:1902.07527 [gr-qc].
- [49] C. D. Capano, M. Cabero, J. Westerweck, J. Abedi, S. Kastha, A. H. Nitz, Y.-F. Wang, A. B. Nielsen, and B. Krishnan, Phys. Rev. Lett. **131**, 221402 (2023), arXiv:2105.05238 [gr-qc].
- [50] T. Accadia et al., Class. Quant. Grav. **27**, 194011 (2010).
- [51] S. Soni et al. (LIGO), Class. Quant. Grav. **38**, 025016 (2020), arXiv:2007.14876 [astro-ph.IM].
- [52] D. Davis et al. (LIGO), Class. Quant. Grav. **38**, 135014 (2021), arXiv:2101.11673 [astro-ph.IM].
- [53] A. E. Tolley, G. S. Cabourn Davies, I. W. Harry, and A. P. Lundgren, Class. Quant. Grav. **40**, 165005 (2023), arXiv:2301.10491 [gr-qc].
- [54] B. P. Abbott et al. (LIGO Scientific, Virgo), Phys. Rev. Lett. **121**, 161101 (2018), arXiv:1805.11581 [gr-qc].
- [55] B. P. Abbott et al. (LIGO Scientific, Virgo), Phys. Rev. X **9**, 031040 (2019), arXiv:1811.12907 [astro-ph.HE].
- [56] R. Abbott et al. (LIGO Scientific, Virgo), Phys. Rev. X **11**, 021053 (2021), arXiv:2010.14527 [gr-qc].
- [57] C. Cutler and J. Harms, Phys. Rev. D **73**, 042001 (2006), arXiv:gr-qc/0511092.
- [58] K. Chatziioannou, C.-J. Haster, T. B. Littenberg, W. M. Farr, S. Ghonge, M. Millhouse, J. A. Clark, and N. Cornish, Phys. Rev. D **100**, 104004 (2019), arXiv:1907.06540 [gr-qc].
- [59] C. Plunkett, S. Hourihane, and K. Chatziioannou, Phys. Rev. D **106**, 104021 (2022), arXiv:2208.02291 [gr-qc].
- [60] B. Allen, Phys. Rev. D **71**, 062001 (2005), arXiv:gr-qc/0405045.
- [61] S. A. Usman et al., Class. Quant. Grav. **33**, 215004 (2016), arXiv:1508.02357 [gr-qc].
- [62] D. Davis, L. V. White, and P. R. Saulson, Class. Quant. Grav. **37**, 145001 (2020), arXiv:2002.09429 [gr-qc].
- [63] S. Vitale, D. Gerosa, C.-J. Haster, K. Chatziioannou, and A. Zimmerman, Phys. Rev. Lett. **119**, 251103 (2017), arXiv:1707.04637 [gr-qc].
- [64] S. Ghonge, K. Chatziioannou, J. A. Clark, T. Littenberg, M. Millhouse, L. Cadonati, and N. Cornish, Phys. Rev. D **102**, 064056 (2020), arXiv:2003.09456 [gr-qc].
- [65] J. Heinzl, C. Talbot, G. Ashton, and S. Vitale, Mon. Not. Roy. Astron. Soc. **523**, 5972 (2023), arXiv:2304.02665 [astro-ph.HE].
- [66] C. R. Harris, K. J. Millman, S. J. van der Walt, R. Gommers, P. Virtanen, D. Cournapeau, E. Wieser, J. Taylor, S. Berg, N. J. Smith, R. Kern, M. Picus, S. Hoyer, M. H. van Kerkwijk, M. Brett, A. Haldane, J. F. del Río, M. Wiebe, P. Peterson, P. Gérard-Marchant, K. Sheppard, T. Reddy, W. Weckesser, H. Abbasi, C. Gohlke, and T. E. Oliphant, Nature **585**, 357 (2020).
- [67] P. Virtanen, R. Gommers, T. E. Oliphant, M. Haberland, T. Reddy, D. Cournapeau, E. Burovski, P. Peterson, W. Weckesser, J. Bright, S. J. van der Walt, M. Brett, J. Wilson, K. J. Millman, N. Mayorov, A. R. J. Nelson, E. Jones, R. Kern, E. Larson, C. J. Carey, Í. Polat, Y. Feng, E. W. Moore, J. VanderPlas, D. Laxalde, J. Perktold, R. Cimrman, I. Henriksen, E. A. Quintero, C. R. Harris, A. M. Archibald, A. H. Ribeiro, F. Pedregosa, P. van Mulbregt, and SciPy 1.0 Contributors, Nature Methods **17**, 261 (2020).
- [68] J. D. Hunter, Computing in Science & Engineering **9**, 90 (2007).
- [69] LIGO Scientific Collaboration, Virgo Collaboration, and KAGRA Collaboration, “LVK Algorithm Library - LAL-Suite,” Free software (GPL) (2018).
- [70] D. M. Macleod, J. S. Areeda, S. B. Coughlin, T. J. Massinger, and A. L. Urban, SoftwareX **13**, 100657 (2021).
- [71] A. M. Price-Whelan et al. (Astropy Collaboration), Astrophys. J. **935**, 167 (2022), arXiv:2206.14220 [astro-ph.IM].
- [72] A. Nitz, I. Harry, D. Brown, C. M. Biwer, J. Willis, T. D. Canton, C. Capano, T. Dent, L. Pekowsky, G. S. C. Davies, S. De, M. Cabero, S. Wu, A. R. Williamson, B. Machenschalk, D. Macleod, F. Pannarale, P. Kumar, S. Reyes, dfinstad, S. Kumar, M. Tápai, L. Singer, P. Kumar, veronica villa, maxtrevor, B. U. V. Gadre, S. Khan, S. Fairhurst, and A. Tolley, “gwastro/pycbc: v2.3.3 release of pycbc,” (2024).
- [73] D. Macleod, E. Goetz, D. Davis, J. Bidler, J. Smith, M. Lowry, siddharth soni, A. Macedo, J. Lynam, katerinaleman, S. Coughlin, A. Lundgren, L. Cotnoir, and T. Massinger, “gwdetchar/gwdetchar: 2.2.7,” (2024).
- [74] R. Abbot et al. (LIGO Scientific Collaboration and Virgo Collaboration and KAGRA Collaboration), “GWTC-3: Compact Binary Coalescences Observed by LIGO and Virgo During the Second Part of the Third Observing Run — Glitch modelling for events,” (2021).
- [75] R. Udall, S. Hourihane, S. Miller, D. Davis, K. Chatziioannou, M. Isi, and H. Deshong, “Data for ”anti-aligned spin of gw191109: Glitch mitigation and its implications”,” (2025).
- [76] R. Macas and A. Lundgren, Phys. Rev. D **108**, 063016 (2023), arXiv:2306.09019 [gr-qc].
- [77] S. Yamamura, H. Yuzurihara, T. Yamamoto, and T. Uchiyama, (2024), arXiv:2403.12731 [gr-qc].
- [78] R. A. Fisher, Statistical methods for research workers, 5 (Oliver and Boyd, 1928).